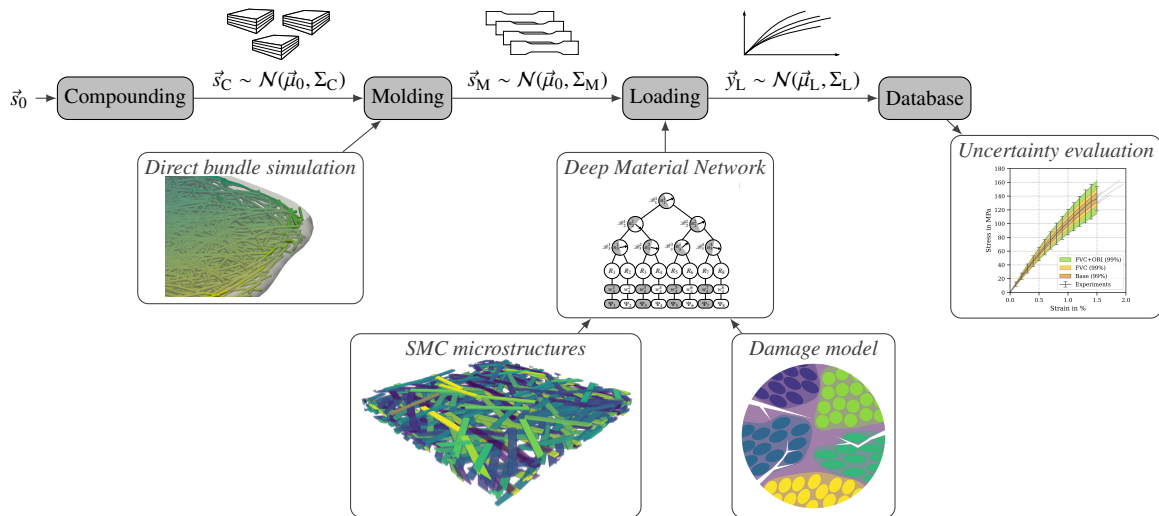


Graphical Abstract

A probabilistic virtual process chain to quantify process-induced uncertainties in Sheet Molding Com- pounds

Nils Meyer, Sebastian Gajek, Johannes Görthofer, Andrew Hrymak, Luise Kärger, Frank Henning, Matti Schneider, Thomas Böhlke



A probabilistic virtual process chain to quantify process-induced uncertainties in Sheet Molding Compounds

Nils Meyer^a, Sebastian Gajek^b, Johannes Görthofer^b, Andrew Hrymak^d, Luise Kärger^a, Frank Henning^{a,c},
Matti Schneider^b, Thomas Böhlke^b

^a*Institute of Vehicle Systems Technology - Division Lightweight Technology, Karlsruhe Institute of Technology (KIT), Rintheimer Querallee 2, Karlsruhe, 76131, Baden-Württemberg, Germany*

^b*Institute of Engineering Mechanics - Chair for Continuum Mechanics, Karlsruhe Institute of Technology (KIT), Kaiserstraße 10, Karlsruhe, 76131, Baden-Württemberg, Germany*

^c*Fraunhofer Institute for Chemical Technology ICT, Joseph-von-Fraunhofer Straße 10, Pfinztal, 76327, Baden-Württemberg, Germany*

^d*Department of Chemical and Biochemical Engineering, University of Western Ontario (UWO), 1151 Richmond Street, London, N6A 5B9, Ontario, Canada*

Abstract

The manufacturing process of Sheet Molding Compound (SMC) influences the properties of a component in a non-deterministic fashion. To predict this influence on the mechanical performance, we develop a virtual process chain acting as a digital twin for SMC specimens from compounding to failure. More specifically, we inform a structural simulation with individual fields for orientation and volume fraction computed from a direct bundle simulation of the manufacturing process. The structural simulation employs an interpolated direct deep material network to upscale a tailored SMC damage model. We evaluate hundreds of virtual specimens and conduct a probabilistic analysis of the mechanical performance. We estimate the contribution to uncertainty originating from the process-induced inherent random microstructure and from varying initial SMC stack configurations. Our predicted results are in good agreement with experimental tensile tests and thermogravimetric analysis.

Keywords: C. Micro-mechanics, C. Numerical analysis, C. Statistical properties, E. Compression Molding, Virtual process chain

Email address: nils.meyer@kit.edu (Nils Meyer)

1. Introduction

1.1. State of the art

Sheet Molding Compound (SMC) is a discontinuous fiber reinforced polymer material that is available in the form of sheets which are pre-impregnated with a thermoset resin. The manufacturing process leads to a random planar orientation distribution of bundled fibers in the prepreg sheets. These sheets are cut and stacked to form an initial charge that is subsequently molded to a part in a compression molding process. The resulting SMC parts have superior mechanical properties in comparison to injection molded parts due to their higher fiber length while maintaining the ability to fill complex geometrical features due to the flow process during compression molding. However, the manufacturing process leads to a spatially varying fiber configuration, i.e., an inhomogeneous fiber volume fraction and anisotropic fiber orientation, which determines the properties of a resulting part [1, 2].

The fiber configuration found in SMC components is a complex three-dimensional arrangement of fiber bundles. As an efficient description, we may define appropriate microstructure characteristics to describe the properties within a region, such as the fiber volume fraction f and the (second-order) fiber orientation tensor \mathbf{A} [3]. For curved SMC fiber bundles, we use a length-weighted second-order fiber orientation tensor

$$\mathbf{A} = \frac{1}{L} \sum_{i=1}^N \int_0^{L_i} \mathbf{p}_i(s) \otimes \mathbf{p}_i(s) ds \quad \text{with} \quad L = \sum_{i=1}^N L_i \quad (1)$$

for N fibers, each of which is described with a varying direction $\mathbf{p}_i(s) \in \mathbb{R}^3$ along its arc length $s \in [0, L_i]$ [4].

Virtual process chains for composite materials are used to address the coupling between manufacturing, the resulting microstructure and the mechanical performance in an early virtual product development stage. These virtual process chains integrate manufacturing simulations to inform structural simulations about the fiber orientation state after molding [5, 6, 7]. While previous virtual process chains increased accuracy of structural simulations in a deterministic fashion, typically they are not able to quantify uncertainty of the predicted processing effects. Indeed, in SMC components, even for simple geometries, there is a significant variation in terms of the underlying microstructure, described by the fiber volume fraction f and the fiber orientation tensor \mathbf{A} , between individual realizations due to the randomness of the prepreg manufacturing process [8, 9, 10]. Accounting for such effects is imperative to fully exploit the lightweight potential of composite materials by reducing safety factors.

The effect of a stochastic microstructure on mechanical performance of SMC has been addressed for example by Chen et al. [11] in a multiscale framework using a stochastic microstructure reconstruction algorithm and a Kriging model for scale bridging. However, the authors did not consider propagation of uncertainties from the molding simulation and used a macroscopic process simulation with fixed fiber volume fraction instead of directly simulating the motion of individual fiber bundles. Mansour et al. [12] analyzed the inherent randomness and size dependent properties in thin fiber networks constituting the microstructure of paper. They use

stochastic volume elements to derive a statistically equivalent stochastic effective constitutive model for paper from direct micromechanical simulations. Their model is based on correlated random fields for modeling the spatially distributed strength and strain fields, which are constructed from multivariate kernels. However, the damage mechanisms and microstructures in paper are vastly different to polymer composites and their work is limited to isotropic orientation distributions. Sommer et al. [13] investigated the variable properties of stochastic prepreg platelet molded composites (PPMC). They analyze the process-structure-property relationships for the stochastic microstructure by experimental methods and by linking a smoothed particle hydrodynamics (SPH) flow simulation with a progressive failure model. However, they simulate only few realizations and assume constant fiber volume fraction (no resin pockets).

1.2. Contribution

In this work, we propose a framework for estimating the stochastic outcomes of a virtual SMC process chain. To address uncertainty in SMC components, we enhance our previous virtual process chain [7] in three areas:

1. We utilize a more capable direct process simulation that represents fiber bundles directly by truss elements which interact with the matrix through hydrodynamic forces [14, 15, 16, 17, 10]. Contrary to macroscopic simulation models, the former allows us to compute multiple realizations of a molding process with different stochastic bundle structures. Further, the improved process model allows to evaluate a spatially varying fiber volume fraction field in addition to the fiber orientation field.
2. We utilize a convex and anisotropic damage model that takes the characteristic bundle microstructure of SMC composites [18] into account via dedicated extraction tensors [19]. Our framework enables to combine different damage functions in a modular way to capture any anisotropic damage evolution. Motivated by Puck's laminate criteria, we developed different extraction tensors for specific damage cases present in the SMC composite. Directly operating on the compliance tensor as primary damage variable in combination with a set of physically meaningful damage parameters yields a well-posed model with which we can accurately capture the damage evolution on the microscale [20].
3. For conducting two-scale simulations of SMC components, we use the framework of direct deep material networks [21, 22, 23, 24] which we augment by a fiber orientation and fiber volume fraction interpolation scheme. In contrast to previous works [22], this approach allows to accurately resolve the spatially varying fiber volume fraction as well as the spatially varying fiber orientation in a component scale simulation.

These individual contributions, i.e., a direct process simulation approach, an accurate constitutive model for anisotropic damage in SMC and a versatile upscaling approach, form an enhanced virtual process chain. Notably, our enhanced process chain accounts for both fiber orientation and fiber volume fraction by a direct

evaluation of the bundle structure on a structural simulation mesh. The efficient implementation and upscaling enables us to compute hundreds of macroscopic virtual specimens with individual spatially varying fiber configurations. We vary the initial stack configuration in terms of the overall fiber volume fraction and overall fiber orientation while keeping material parameters and boundary conditions constant. For each variation, we compute multiple realizations of SMC components and analyze these to understand sources of process-induced uncertainties. Eventually, this allows a further reduction in safety factors to exploit the full lightweight potential of SMC parts.

The virtual process chain is described in Section 2 for the three individual contributions *compression molding simulation*, *damage modeling* and *upscaling*. In Section 3, we apply the methods to establish a database of virtual tensile tests for a plate molding process. In Section 4, we evaluate the results in this database to estimate uncertainties in the mechanical response depending on specimen size and prepreg properties. Finally, we compare our predictions to the scattering observed in previously reported experiments [25].

2. A virtual process chain for Sheet Molding Compounds

2.1. Concept

We design a virtual process chain which is a continuous digital representation of a specimen's life from semi-finished raw materials up to its end of life due to failure in a testing rig. Such a virtual process chain of an SMC specimen is schematically illustrated in Figure 1.

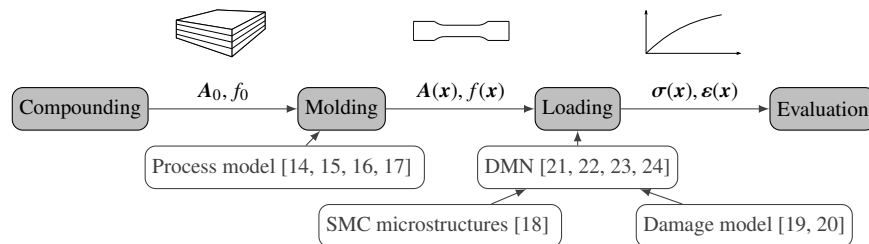


Figure 1: Schematic representation of the virtual SMC process chain for a single realization with nominal initial fiber orientation state A_0 and nominal initial fiber volume fraction f_0

The starting point of the virtual SMC process chain is the configuration of a prepreg sheet stack, which is placed at a dedicated position in a mold. The sheets in this stack have an initial fiber configuration described by the second-order fiber orientation tensor A_0 (see equation (1)) and the initial fiber volume fraction f_0 . A process simulation computes the change of the initial fiber configuration during a compression molding process and predicts the locally distributed orientation states $A(x)$ and fiber volume fractions $f(x)$ after the manufacturing process. These fields serve as an input to a structural simulation to compute the tensile stress σ , the tensile strain ϵ and the damage in the specimen due to loading.

2.2. Compression molding simulation

Traditional macroscopic approaches. A compression molding simulation of SMC describes the mold filling process starting from an initial SMC stack until the mold is completely filled. The process may be decomposed into three steps [26]: An initial *squish phase* with a complex flow front and a release of entrapped air in the stack, a stable *plug-flow* with an extensional flow of SMC and a final *boiling phase* after complete mold closing. The plug-flow is the dominant kinematic flow mechanism during SMC compression molding. The plug-flow kinematic was first shown by Barone and Caulk [27], who suggested that the heated resin near mold walls forms a thin lubrication layer that is best described by hydrodynamic friction models [28]. Calibrated models for the hydrodynamic friction in SMC plug-flows and more advanced friction models for it are available [29, 30, 31]. As the flow phase is short compared to the time scale of curing and heat transfer, simulation models often simplify the process model to be isothermal without curing, such that the heated lubrication layer is only accounted for through the friction model between mold and SMC [30, 31]. The fiber orientation is typically described by an evolution equation for the second-order fiber orientation tensor, which was introduced by Advani and Tucker [3] as an efficient numerical treatment for spatially varying fiber-orientation distributions and is based on Jeffery’s equation [32]. There are approaches to account for varying fiber volume content during processing [33, 34, 35], but most macroscopic compression molding simulations assume a constant fiber volume fraction.

Instead of solving effective measures like fiber orientation tensors or fiber volume fractions, one may directly simulate the motion of individual fiber bundles during the compression molding process [14, 15]. The key here is the observation that fiber bundles often stay intact during molding [36, 37, 38], which allows us to treat hundreds of fibers as individual bundle instances. This reduces the computational effort significantly and allows for a direct simulation of all flexible bundles in entire parts of industrial complexity with up to 250 000 bundles [16].

A direct bundle simulation approach for the molding process. The process simulation model solves conservation of mass, momentum and internal energy in a Coupled Eulerian Lagrangian (CEL) framework [39], where each Eulerian element is attributed an Eulerian volume fraction $e \in [0, 1]$. The motion of SMC in the Eulerian phase is driven by molds that are modeled as rigid bodies and are in contact with the reconstructed SMC surface [40].

The core idea of the direct bundle simulation approach is the treatment of fiber bundles as one dimensional flexible objects represented by truss elements (i.e., one dimensional elements that transfer axial forces only) which interact with a viscous matrix via a body force field in the CEL momentum equation [14]. Initially, these truss elements are generated in the region of the SMC stack by drawing random directions from a uniform distribution on a unit sphere, which are then projected to a planar isotropic orientation state \mathbf{A}_0 , shifted randomly within the stack and cut if extending outside the stack (see Section Appendix A for details and [18] for a comprehensive overview). This procedure results in a realization of a random process similar to the sheet

manufacturing and introduces a length distribution due to cut fiber bundles at the edges of the stack similar to the physical cutting process of sheets.

During the flow process, the matrix is modeled as a compressible viscous material with an equation of state fitted to compaction trials and a Cross-WLF viscosity model [17]. Each truss element experiences a hydrodynamic drag force from the surrounding matrix that is proportional to the relative velocity of the surrounding matrix [14]. The relative velocity is computed from weighted neighboring elements and an opposed body force field is applied to those neighbors ensuring a two-way coupled anisotropic flow [14].

The tangential hydrodynamic mold friction causes a shear stress traction vector at the mold surface $\boldsymbol{\tau} \in \mathbb{R}^2$ that follows a power-law model

$$\boldsymbol{\tau} = -\lambda \left(\frac{\|\boldsymbol{v}_s\|}{v_0} \right)^{m-1} \boldsymbol{v}_s, \quad (2)$$

where $\lambda \in \mathbb{R}_{>0}$ is a hydrodynamic friction coefficient, $m \in [0, 1]$ is a power-law coefficient, $v_0 \in \mathbb{R}_{>0}$ is an arbitrary reference velocity for non-dimensionalization, and $\boldsymbol{v}_s \in \mathbb{R}^2$ is the slip velocity at the mold surface [30, 41]. For the thermal contact we assume that the heat flux is proportional to the difference between SMC temperature and the mold temperature with a gap conductance $K_T \in \mathbb{R}_{>0}$ [17].

Evaluation of process simulation results. When using a direct bundle simulation, the fiber-bundle statistics are readily computable in post-processing. The fiber-bundle statistics may be transferred to virtual specimens with data about fiber orientation as well as fiber volume fraction. In contrast to mapping methods, which may introduce interpolation errors to the model [42], we evaluate the bundle configuration directly in each cell of the target mesh and thus ensure coherent and natural correlations between cells. The fiber volume fraction in cell a is approximated as

$$f_a = A_B \sum_{i \in \mathcal{B}_a} \frac{\Delta l_{ai}}{V_a}, \quad (3)$$

where \mathcal{B}_a contains all truss elements crossing cell a and A_B denotes the cross section area of a bundle. The length of bundle element i within a cell a is denoted Δl_{ai} and the cell volume is V_a . Similarly, the second-order discrete fiber orientation tensor is computed as

$$\boldsymbol{A}_a = \frac{1}{L_a} \sum_{i \in \mathcal{B}_a} \Delta l_{ai} \boldsymbol{p}_i \otimes \boldsymbol{p}_i \quad \text{with} \quad L_a = \sum_{i \in \mathcal{B}_a} \Delta l_{ai} \quad (4)$$

and the bundle orientation \boldsymbol{p}_i .

2.3. Structural damage modeling

Current state of research. Damage modeling is devoted to the continuum description of progressive stiffness degradation on the macroscale due to the growth of defects such as voids or microcracks on a lower length scale [43, 44]. Two general approaches have prevailed, phenomenological models in combination with suitable kinetic laws operating on the macroscale [45, 46] and micromechanics-based models directly taking into account

the damage mechanisms on the microscale [47, 48, 20]. The latter allow for an easier handling of microstructural stochastics such as uncertainty in the elastic properties of fiber reinforced concrete [49], random loading in fatigue processes [50], progressive fiber breakage [51, 52], interfacial effects and strength [53, 11] or localized microcracks [54].

Depending on the state of anisotropy induced by progressive damage, different damage model approaches are used: Scalar-valued damage approaches to describe isotropic stiffness degradation, as e. g., used to model steel-fiber reinforced concrete [55], fiber reinforced plastic composite plies [56], or notched epoxy resin specimens [57]. Second-order damage tensors are used to model orthotropic stiffness degradation due to damage evolution [58]. Especially in the field of composite research, these approaches are frequently applied, e. g., to describe composite fabrics and laminated panels [59], composite laminates [60, 61] or ceramic-matrix composites [62]. At least a fourth-order damage tensor is necessary to capture any anisotropic stiffness degradation [45, section 4]. Indeed, an approach operating on the stiffness or compliance tensor as primary damage variable seems natural. Some applications include modeling of concrete [63, 64, 65] and elasto-plasticity coupled to damage [66, 67].

When used to describe softening material behavior, local damage model formulations generally become ill-posed due to localization effects [44], which lead to strongly mesh-dependent results [68]. Solution approaches include non-local formulations [69, 70] such as gradient enhancements [71, 72, 73], convolution with a tapering function [74] or an augmentation via an elliptic differential operator [75]. Other approaches, inter alia, apply relaxation techniques to the local damage formulation as a countermeasure [76, 77, 78]. For a summary on ill-posedness and regularization methods, we refer to Forest et al. [79].

As long as the material behavior is dominated by a hardening regime, locally formulated damage material models remain well-posed. An approach that reflects this entire class of hardening-type materials and is able to capture any anisotropic stiffness degradation due to damage evolution was introduced by Görthofer et al. [19]. We apply the model to SMC using specific adaptations to capture matrix and bundle damage.

A convex damage model for hardening-type materials. We formulate the model in the setting of generalized standard materials [80] with a free energy density $\psi : \text{Sym}(3) \times S \times Q \rightarrow \mathbb{R}$ which is comprised of an elastic part and a part related to damage. The elastic part is defined on the space of symmetric 3×3 strain tensors $\boldsymbol{\varepsilon} \in \text{Sym}(3)$. Furthermore, the model directly operates on the space of symmetric and positive definite compliance tensors $\mathbb{S} \in S = \{\mathbb{S} \in \text{Sym}(\text{Sym}(3)) \mid \boldsymbol{\tau} \cdot \mathbb{S}[\boldsymbol{\tau}] > 0 \quad \forall \boldsymbol{\tau} \in \text{Sym}(3) \setminus \{0\}\}$ as the primary damage variable and a set of general variables $q \in Q$ describing the shape and size of the damage surfaces. Whereas the domain Q may in general be abstract, we will utilize damage-activation functions (see equation (7)) so that $Q \equiv \mathbb{R}^M$ with M being the number of different damage cases. With the classical linear elastic energy density

and a power-law ansatz for the damage part, we introduce the free energy density ψ as

$$\psi(\boldsymbol{\varepsilon}, \mathbb{S}, q) = \frac{1}{2} \boldsymbol{\varepsilon} \cdot \mathbb{S}^{-1} [\boldsymbol{\varepsilon}] + \sum_{i=1}^M \frac{H_i}{m_i + 1} q_i^{m_i+1}, \quad (5)$$

with hardening parameters $H_i \in \mathbb{R}_{>0}$ and exponents $m_i \in \mathbb{R}_{>0}$. Suitably, we introduce the force potential Φ^* in terms of M convex damage-activation functions g that bound the elastic regime in analogy to associated elasto-plastic models. Directly integrating the driving forces for the compliance \mathbb{S} and the damage variables q , we formulate the force potential $\Phi^* : \text{Sym}(3) \times Q \rightarrow \mathbb{R} \cup \{+\infty\}$ in its simplified version

$$\Phi^*(\boldsymbol{\sigma}, q) = \begin{cases} 0, & g_i(\boldsymbol{\sigma}, q_i) \leq 0, \quad \forall i = 1, \dots, M, \\ +\infty, & \text{else,} \end{cases} \quad (6)$$

The damage-activation functions (see equation (7)) take the current stress state into account. For damage to evolve, this stress state has to exceed a damage-activation threshold $\sigma_{0,i} \in \mathbb{R}_{>0}$ in combination with a part accounting for the onset of damage

$$g_i(\boldsymbol{\sigma}, q_i) = \|\mathbb{B}_i[\boldsymbol{\sigma}]\|^2 - \sigma_{0,i}^2 - H_i^2 q_i^{m_i}. \quad (7)$$

Case-specific stresses are extracted via dedicated extraction tensors \mathbb{B}_i that can be tailored to the application at hand. Via Biot's dual equation [81] we determine the evolution equations for the internal variables and the associated Karush-Kuhn-Tucker (KKT) conditions [82, 83]. Eventually, a proper reformulation yields the compliance for any state of damage captured by the associated damage variables

$$\mathbb{S} = \mathbb{S}_0 + 2 \sum_{i=1}^M \frac{q_i}{H_i} \mathbb{B}_i^2, \quad (8)$$

where \mathbb{S}_0 is the initial compliance. The corresponding KKT conditions have the form

$$g_i(\boldsymbol{\sigma}, q_i) \leq 0, \quad \dot{q}_i \geq 0, \quad \dot{q}_i g_i(\boldsymbol{\sigma}, q_i) = 0, \quad i = 1, \dots, M. \quad (9)$$

The model is thermodynamically consistent and satisfies Wulfhinghoff's damage growth criterion [84]. Furthermore, it can be applied to any hardening-type damage material. An efficient predictor-corrector framework in analogy to problem settings in elasto-plasticity allows for an efficient computation. For a detailed overview on the model, the reader is referred to the original publication [19].

Extraction tensors to describe damage in SMC composites. A variety of concurring experimental investigations [85, 86, 87, 88] show matrix and bundle damage to be the dominant damage mechanisms in SMC composites. To capture damage onset in the matrix, we implement the extraction tensor

$$\mathbb{B}_M = \frac{1}{3} \mathbf{I} \otimes \mathbf{I}, \quad (10)$$

accounting for damage due to dilatation [20]. Motivated by Puck’s criteria for laminates [89, 90], we derive extraction tensors for bundle damage that capture normal stresses perpendicular to the bundle direction and shear stresses in bundle direction [19, 20]. Using a maximum stress approach based on a pencil glide ansatz [91, 92], we implement the associated extraction tensors as

$$\mathbb{B}_{B,N} = \frac{\sqrt{2}}{2} (\mathbf{e}_2^{\otimes 2} + \mathbf{e}_3^{\otimes 2})^{\otimes 2} + \frac{\sqrt{2}}{4} (\mathbf{e}_2^{\otimes 2} - \mathbf{e}_3^{\otimes 2})^{\otimes 2} + (\mathbf{e}_2 \otimes_S \mathbf{e}_3)^{\otimes 2} \quad (11)$$

and

$$\mathbb{B}_{B,S} = (\mathbf{e}_1 \otimes_S \mathbf{e}_2)^{\otimes 2} + (\mathbf{e}_1 \otimes_S \mathbf{e}_3)^{\otimes 2}, \quad (12)$$

with orthonormal basic vectors \mathbf{e}_1 , \mathbf{e}_2 and \mathbf{e}_3 . For better clarity, we use the abbreviations $\mathbf{a}^{\otimes n} = \mathbf{a} \otimes \mathbf{a} \dots \mathbf{a}$ (n repetitions) and $\mathbf{a} \otimes_S \mathbf{b} = (\mathbf{a} \otimes \mathbf{b} + \mathbf{b} \otimes \mathbf{a}) / 2$ for any vectors $\mathbf{a}, \mathbf{b} \in \mathbb{R}^3$.

As each damage-activation function g_i is comprised of one extraction tensor \mathbb{B}_i and three damage parameters $(\sigma_{0,i}, H_i, m_i)$, we have to determine a set of 9 parameters to describe the anisotropic damage evolution of our SMC composite.

2.4. An efficient upscaling approach using deep material networks

Current state of research. Two-scale simulation approaches are a powerful tool for the analysis of microstructured materials. If the microstructure inhomogeneities fluctuate on a scale much smaller than the actual component, homogenization techniques may be used to obtain effective material models. The former emerge by solving a partial differential equation, the cell problem of first order homogenization. Such an effective model accounts for the physical mechanisms of the microstructure and the nonlinear behavior of the constituents in a macroscopic simulation.

The approach of solving the cell problem on a finite element (FE) model of the underlying microstructure as well as in every Gauss point of a macroscopic finite element simulation is commonly referred to as the FE² method [93, 94, 95]. Similar in spirit, but relying on a fast Fourier-transform (FFT) based micromechanics solver [96, 97, 98], the FE-FFT method [99, 100] was introduced. Both the FE² and FE-FFT method provide excellent accuracy which comes at the expense of considerable computational costs, limiting their practicality for problems of industrial complexity. As a remedy, model order reduction techniques, i.e., the transformation field analysis (TFA) [101, 102, 103], the self-consistent clustering analysis (SCA) [104, 105, 106] or the non-uniform transformation field analysis (NTFA) [107] seek to approximate the solution of the cell problem. However, the weak approximation qualities of piece-wise uniform functions give rise to a slow convergence rate of the TFA and SCA in terms of the number of used clusters [108, 109]. This problem is mitigated in the NTFA by relying upon non-uniform basis functions for the inelastic strains. However, the difficulty is then transferred to prescribing suitable evolution equations [110, 111].

Furthermore, data-driven approaches relying on feed-forward neural networks [112, 113, 114] or recurrent neural networks [115, 116, 117] discard with micromechanics and seek to approximate the effective stress-strain

relationship of the microstructure and constituents. Nevertheless, as powerful as these data-driven approaches are, accounting for inherent physical properties, preservation of thermodynamic consistency and stress-strain monotonicity, especially far away from the training domain, may be difficult.

Liu and co-workers [118, 119] introduced deep material networks (DMNs), a micromechanics inspired data-driven modeling approach relying on nested laminates, which serve as high-fidelity surrogate models for full-field simulations on microstructures with inelastic constituents. Gajek et al. [21] introduced direct DMNs with a reduced number of fitting parameters to be identified also allowing for an efficient implementation in a two-scale context [22, 23, 24]. In contrast to approximating the effective stress-strain relationship, DMNs seek to replace the underlying microstructure by a surrogate model which dispenses with a physical representation but retains positive characteristics, i.e., preservation of fundamental micromechanical bounds, preservation of thermodynamical consistency and monotonicity or fulfillment of the Hill-Mandel condition, see Gajek et al. [21] for a discussion. Furthermore, the associated cell problem can be solved efficiently and can easily be extended to account for other physical effects, e.g., to account for thermodynamical coupling [24] in a two-scale setting.

Micro-oriented direct deep material networks. In their original formulation, two-phase direct DMNs [21] were introduced as perfect, ordered, rooted binary trees of laminates. More precisely, every node of the binary tree is given by a two-phase, rank-one laminate building block \mathcal{B}_k^i (k indexes the depth and i designates the horizontal position), see Figure 2. However, this formulation is restricted to microstructures without micro-oriented phases, i.e., considering anisotropic SMC bundles as second phase beside the isotropic unsaturated polyester polyurethane hybrid (UPPH) matrix (see Bücheler [120] for information on the material system) is not possible. Thus, we augment the direct DMN framework [21, 22, 23, 24] with an additional rotation layer at the bottom of the binary tree, enabling the treatment of micro-oriented problems.

On a more formal level, we consider a micro-oriented direct DMN of two phases in three spatial dimensions and of depth K to consist of the following.

1. A vector $\vec{\mathbf{n}} = [\mathbf{n}_K^1, \mathbf{n}_K^2, \dots, \mathbf{n}_1^2, \mathbf{n}_1^1] \in \mathcal{N} := (\mathbb{R}^3)^{2^K-1}$ comprising the lamination directions of all laminate building blocks inserted in a reversed breadth-first ordering.
2. A vector of non-negative weights $\vec{w} = [w_{K+1}^1, w_{K+1}^2, \dots, w_{K+1}^{2^K}] \in \mathcal{W} := \mathbb{R}_{\geq 0}^{2^K}$, summing to unity, which are used to parameterize the volume fractions of all laminate blocks, see Gajek et al. [21] or Liu et al. [118] for more details.
3. A vector of rotation matrices $\vec{\mathbf{R}} = [\mathbf{R}_1, \dots, \mathbf{R}_{2^K}] \in \mathcal{R} := SO(3)^{2^K}$ specifying the material orientation.

The vector of lamination directions $\vec{\mathbf{n}}$, the vector of weights \vec{w} and the vector of rotation matrices $\vec{\mathbf{R}}$ uniquely determine the direct DMN and serve as the fitting parameters of the surrogate model. Most notably, the DMN is trained on linear elastic training data exclusively. Subsequently, after parameter identification, the DMN is used to extrapolate to the nonlinear regime with astonishing accuracy, see Gajek et al. [21] for more background.

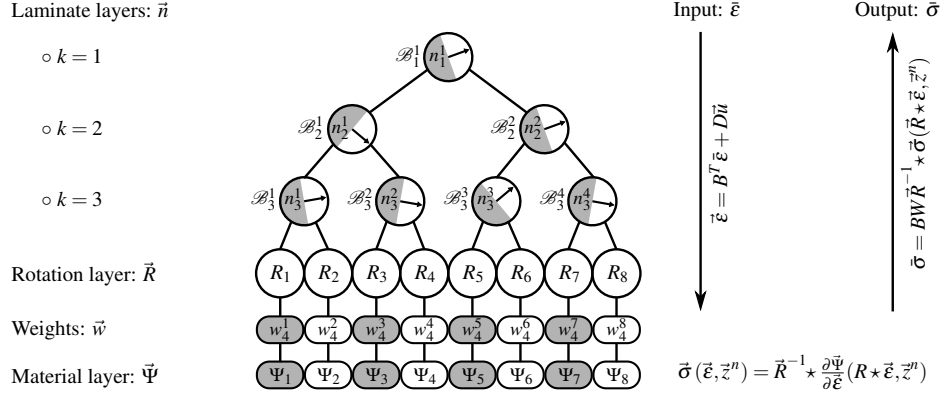


Figure 2: A two-phase direct DMN of depth 3

The parameters $(\vec{n}, \vec{w}, \vec{R})$ only depend on the geometric composition of the underlying microstructure the model is fitted on and are independent of the constituents. However, for many material classes including SMC, the geometric composition of the microstructure (typically described by suitable microstructure characteristics) fluctuates significantly on the macroscopic scale, an effect usually induced by the manufacturing process of the composite. As a consequence, a plethora of parameter sets $(\vec{n}, \vec{w}, \vec{R})$, typically one for every Gauss point of the macroscopic simulation, needs to be identified in order to employ the DMN surrogate model in a two-scale simulation. As a remedy, the interpolation of the parameters $(\vec{n}, \vec{w}, \vec{R})$ has been proposed [22, 121, 122], which assumes that $(\vec{n}, \vec{w}, \vec{R})$ depend continuously on the relevant microstructure characteristics such that only a single parameter identification process is necessary.

Interpolating direct deep material networks. For SMC, the relevant microstructure characteristics are given by the fiber volume fraction and the second-order fiber orientation tensor. In principle, the fiber volume fraction $f \in [0, 1]$ ranges between zero and one. Typically, the maximum fiber content is capped well below one, mainly due to geometric considerations. By general covariance considerations, two fiber orientation states which differ only by an orthogonal transformation should give rise to effective material responses which differ only by this orthogonal transformation [22]. Consequently, restricting to planar fiber orientation states, we may parameterize essentially different fiber orientation states by the following second-order fiber orientation tensor

$$\mathbf{A} \hat{=} \text{diag}(a, 1 - a, 0) \in \mathbb{R}^{3 \times 3} \quad (13)$$

which only depends on a single parameter $a \in [0.5, 1]$ (assuming that the principal fiber orientations coincide with the axes of the underlying SMC microstructure). For instance, for $a = 0.5$, we recover a planar orientation state whereas for $a = 1$ a unidirectional state is observed.

To obtain a surrogate model admissible for any pair (f, a) , we define the (interpolated) parameter vector $\vec{p}(f, a) = [\vec{n}(a), \vec{w}(f), \vec{R}(a)]$. Here, we assume that the directions of lamination $\vec{n}(a)$ and the rotation matrices $\vec{R}(a)$ depend linearly on the fiber orientation parameter a and are independent of the fiber volume fraction f , see

Gajek et al [22] for a suitable parametrization. Furthermore, we assume that the weights $\vec{w}(f)$ are parameterized by an (affine) linear function of the fiber volume fraction f and expressed in terms of the unconstrained weights $\vec{v} \in \mathbb{R}^{2^K}$ (to ensure non-negativity, see also Gajek et al. [21] or Liu et al. [118]), i.e.,

$$w_{K+1}^{2^i}(f) = f \langle v_{2i} \rangle_+ \quad \text{and} \quad w_{K+1}^{2^{i-1}}(f) = (1-f) \langle v_{2i-1} \rangle_+ \quad (14)$$

holds, together with the consistency conditions

$$\sum_{i=1}^{2^{K-1}} \langle v_{2i} \rangle_+ = 1 \quad \text{and} \quad \sum_{i=1}^{2^{K-1}} \langle v_{2i-1} \rangle_+ = 1. \quad (15)$$

Here, $\langle \cdot \rangle_+ : \mathbb{R} \rightarrow \mathbb{R}_{\geq 0}$, $x \mapsto \max(0, x)$, denotes the Macaulay bracket, commonly known as the ReLU activation function in machine learning.

Upscaling with deep material networks. After the parameter identification, for a fixed fiber orientation a and a fixed volume fraction f , given nonlinear laws for the phases and a time discretization by an implicit Euler method, the DMN might be thought of as the mapping $\mathbf{h}_{a,f} : \text{Sym}(3) \times \vec{\mathcal{Z}} \rightarrow \text{Sym}(3)$,

$$\vec{\sigma}^{n+1} = \mathbf{h}_{a,f}(\vec{\epsilon}^{n+1}, \vec{z}^n) \quad (16)$$

which computes an effective stress increment $\vec{\sigma}^{n+1}$ in dependence of the given macroscopic strain increment $\vec{\epsilon}^{n+1}$ and given vector of internal variables \vec{z}^n of the last converged time step. This function can be implemented rather efficiently, enabling the analysis of industrial-scale composite components in a two-scale setting which resolves the fluctuation of f and a on the macroscopic scale. Details on the implementation are summarized in Appendix B.

3. Application to a plaque with tensile specimens

3.1. Experimental investigations

The experimental results used for comparison in this work are taken from Trauth [25]. An unsaturated polyester polyurethane hybrid (UPPH) resin system introduced by Bücheler [120] filled with a nominal E-glass fiber volume fraction of 26 % was used to manufacture SMC plates (458 mm \times 458 mm). The prepreg stacks were placed in the center of the mold with an initial coverage of the molding area of 35 %. After compression molding, five types of specimens were extracted from the plates according to the cutting plan illustrated in Figure 3. The specimen types include circular TGA samples with 25 mm diameter, rectangular specimens with 15 mm width ($R1$) and 30 mm width ($R2$) as well as dog-bone specimens with 15 mm width ($B1$) and 30 mm width ($B2$). The specimens for mechanical testing ($R1$, $R2$, $B1$, $B2$) were subjected to tensile loading in a universal testing machine and loaded until failure. The strain was recorded with an optical system in a gauge section of 70 mm \times 10 mm at the center of the specimens.

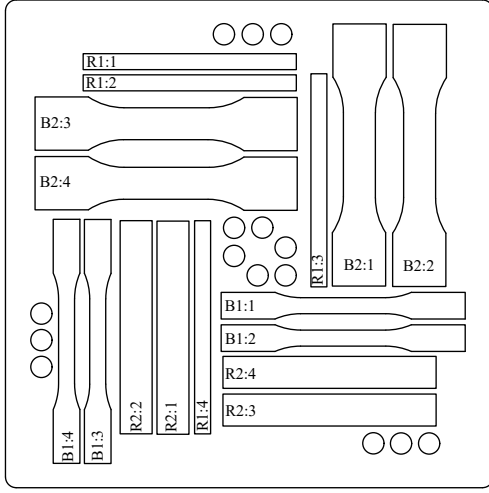


Figure 3: Locations of specimens extracted from molded plates

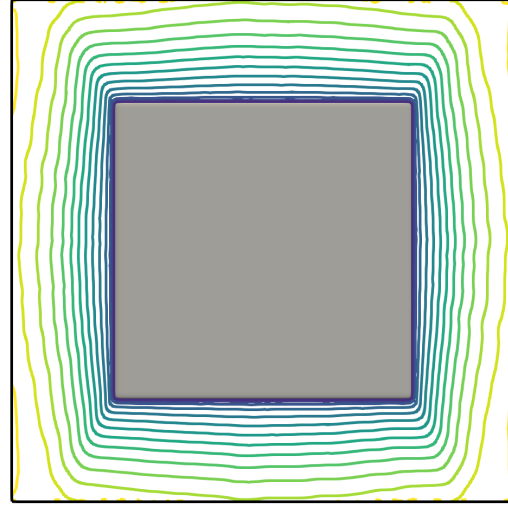


Figure 4: Initial prepreg stack (gray) and contour lines of the filled region at equally spaced time steps

3.2. Compression molding simulation

The compression molding simulation is a transient thermo-mechanical simulation computed in a Coupled Eulerian Lagrangian framework in SIMULIA Abaqus 2021. We model the UPPH matrix as a purely viscous fluid with a Cross-WLF-like equation

$$\eta(T, \dot{\gamma}) = \frac{\eta_0(T)}{1 + \left(\frac{\dot{\gamma}}{\dot{\gamma}_0}\right)^{1-n}} \quad \text{with} \quad \eta_0(T) = D_1 \exp\left(\frac{-\alpha_1(T - T^*)}{\alpha_2 + (T - T^*)}\right), \quad (17)$$

where T is the temperature and $\dot{\gamma} = \sqrt{2\mathbf{D}' : \mathbf{D}'}$ is the scalar shear rate computed from the deviatoric part of the symmetric strain rate tensor \mathbf{D}' . The parameters n , $\dot{\gamma}_0$, T^* , D_1 , α_1 , α_2 are fitted to experimental plate-plate rheometry data [17]. The compressible behavior of the compound, due to air pockets in the prepreg stack, was characterized via compaction trials and we interpolate the measured relation between pressure and volumetric strain during the simulation [17]. The transverse thermal parameters of the compound are determined by fitting the solution of a one-dimensional heat equation to the temperature history of multiple temperature sensors embedded in an SMC stack, which was placed in a hot mold [17]. Molds are represented by isothermal (145 °C) rigid body shells which interact with the surface of SMC via normal contact and hydrodynamic tangential friction. The hydrodynamic mold friction parameters were determined by press rheometry using a compression molding tool equipped with multiple pressure sensors [17]. A summary of parameters for the compression molding simulation is given in Table G.3.

The Eulerian domain is meshed with 670.000 elements of Abaqus type *EC3D8RT* (i.e., linear hexaeders with reduced integration and a temperature degree of freedom) with 1 mm thickness and 2.5 mm in-plane dimensions. The matrix volume fraction in elements is assigned according to the 270 mm × 270 mm × 12 mm sized stack

that is positioned at the center of the mold. The initial stack temperature is set to 25 °C and bundles with 25 mm length are generated in the stack. The bundles are meshed with truss elements of 2.5 mm length and bundles leaving the domain are clipped. The nominal fiber volume content $f_0 \in [0, 1]$ and a nominal planar second-order fiber orientation tensor $\mathbf{A}_0 \hat{=} \text{diag}(a_0, 1 - a_0, 0) \in \mathbb{R}^{3 \times 3}$ with $a_0 \in [0.5, 1]$ in the initial stacks follow Table 1 with four different configurations *A* to *D*.

We compute four different realizations for each configuration with identical nominal properties and compute the mold filling process for each plate realization, i.e., sixteen compression molding simulations in total. The computational setups and computation times are described in Appendix E.1.





| | Nominal volume fraction f_0 | Nominal orientation a_0 | Truss element count | Color Code |
|---|-------------------------------|---------------------------|---------------------|---|
| A | 22.5 % | 0.5 | 1.8 M |  |
| B | 26.0 % | 0.5 | 2.1 M |  |
| C | 29.0 % | 0.5 | 2.4 M |  |
| D | 26.0 % | 0.6 | 2.1 M |  |

Table 1: Investigated initial stack configurations

During molding, the bottom mold remains at rest, while the upper mold is closed by a press controller with a constant velocity $\dot{h} = 3 \text{ mm s}^{-1}$ until a maximum compression force $F_{\max} = 6 \text{ MN}$ is reached. Subsequently the compression force remains constant. The contour lines in Figure 4 show the progress of a compression molding simulation with equally spaced time steps between lines. The gray area in the center indicates the initial prepreg stack placement. The illustration shows a simulation result of configuration *D* with a slight horizontal orientation preference. The compression molding simulation takes the anisotropy into account and predicts faster flow perpendicular to the preferred fiber orientation.

3.3. Structural material parameters

The isotropic elastic phase properties of the E-glass fibers and the UPPH matrix resin system [120] are listed in Table G.4. UPPH was characterized by Trauth, see [25, Section 6.3.1]. Using FFT-based full-field homogenization as well as a Mori-Tanaka mean-field approach [123], we compute the elastic properties of a representative bundle containing 225 unidirectional aligned fibers. Each fiber has a diameter of about 13.5 μm and a length of about 25.4 mm. Based on given μCT scan analyses [124, 125], we assume the volume fraction of fibers within a bundle to be 70 %. The homogenized, transversely isotropic properties of a bundle are summarized in Table G.4.

We identify the parameters describing damage evolution in matrix and bundles (compare Section 2.3) via a Bayesian optimization [126] approach with Gaussian regression [127] as presented in [20]. For the SMC at hand, we fix all power-law exponents m to unity, leaving a set of three damage-activation thresholds σ_0 and three

hardening parameters H to be identified. The identified parameters that minimize the cost-function comparing the experimental and simulation results via a least-square error measure are listed in Table G.5.

3.4. Training of the DMN surrogate model

As discussed in Section 2.4, the space of admissible fiber volume fractions and fiber orientations is given by a continuum $(f, a) \in [0, 1] \times [0.5, 1.0]$ in two dimensions. Before sampling the training data for the linear elastic training, we seek a suitable discretization of our continuum domain. In order to obtain reasonable bounds for these parameters (to keep the computational costs manageable), we analyze the realized fiber volume fractions and fiber orientations occurring as a result of the mold filling simulations. Figure 5 summarizes this information in a heat map representing the frequency of observed fiber orientations and volume fractions.

Please note that local fiber volume fractions of up to 40 % are predicted by the mold filling simulation. However, fiber volume fractions of 35 % correspond to bundle fractions of over 60 % which is close to the theoretical maximum of our random sequential addition (RSA) based SMC microstructure generator [18]. For this reason, we restrict the maximum fiber volume fraction to 35 %. As this limit is exceeded in only about 0.5 % of all cells, we do not expect a significant impact on the macroscale simulations. In addition, we observe a minimum fiber volume fraction of well above 15 %, hence we consider $f \in [0.15, 0.35]$ as suitable. Furthermore, we observe that (close to) unidirectional fiber orientation states do not occur at all. Thus, it suffices to consider fiber orientations $a \in [0.5, 0.8]$ during training as indicated by Figure 5.

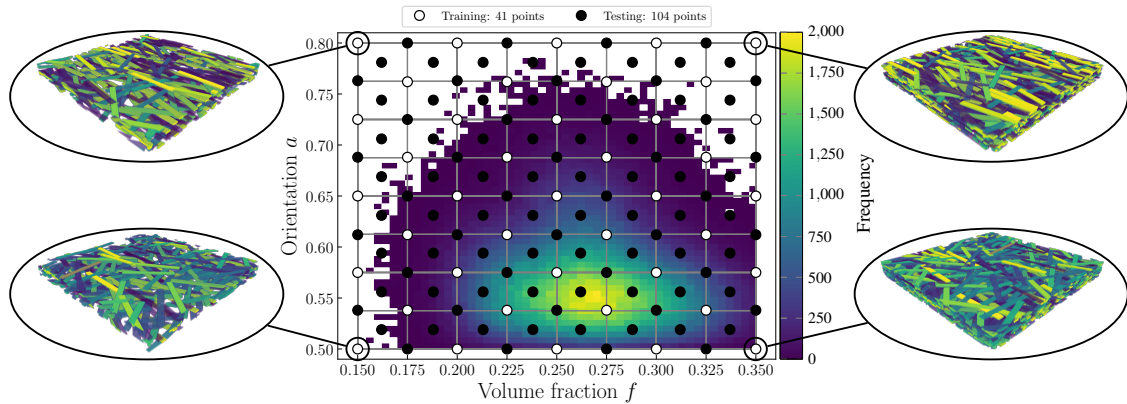


Figure 5: Discretization of the space of admissible fiber volume fraction and fiber orientation and frequencies indicating the prevalence of these after the compression molding simulation

The white dots in Figure 5 represent the 41 tuples $\{(f^s, a^s)\}_{s=1}^{41}$ of our discretized space. We generate an artificial SMC microstructure [18] for any of those tuples. In the next step, we sample $N_s = 1230$ pairs of stiffnesses $(\mathbb{C}_1^s, \mathbb{C}_2^s)$ as explained in Gajek et al. [21], assign each stiffness tuple to one of the generated SMC microstructures in a cyclic fashion, i.e., $(f^s, a^s) \mapsto (f^{(s-1) \bmod 41+1}, a^{(s-1) \bmod 41+1})$, and compute the associated effective stiffness $\bar{\mathbb{C}}^s$ by means of an FFT-based computational micromechanics code as described in Schneider [98].

We randomly split the pre-computed training data $\{(\mathbb{C}_1^s, \mathbb{C}_2^s, \bar{\mathbb{C}}^s, f^s, a^s)\}_{s=1}^{N_s}$ into a training and validation set comprising 80% and 20% of the samples, respectively. The DMN is trained based on the loss function

$$J(\vec{\mathbf{p}}) = \sum_{s=1}^{N_s} J_s(\vec{\mathbf{p}}) + J_p(\vec{\mathbf{p}}) \rightarrow \min_{\vec{\mathbf{p}}} \quad (18)$$

where the first part

$$J_s(\vec{\mathbf{p}}) = \frac{1}{N_s} \frac{\|\mathcal{DMN}_Y^{\mathcal{L}}(\mathbb{C}_1^s, \mathbb{C}_2^s, \vec{\mathbf{p}}(f^s, a^s)) - \bar{\mathbb{C}}^s\|_1}{\|\bar{\mathbb{C}}^s\|_1} \quad (19)$$

measures the proximity of the pre-computed effective stiffness $\bar{\mathbb{C}}^s$ to the DMN's effective stiffness $\bar{\mathbb{C}}_{\text{DMN}}^s = \mathcal{DMN}_Y^{\mathcal{L}}(\mathbb{C}_1^s, \mathbb{C}_2^s, \vec{\mathbf{p}}(f^s, a^s))$. The penalty term

$$J_p(\vec{\mathbf{p}}) = \lambda \left(\sum_{i=1}^{2^{K-1}} \langle v_{2i} \rangle_+ - 1 \right)^2 + \lambda \left(\sum_{i=1}^{2^{K-1}} \langle v_{2i-1} \rangle_+ - 1 \right)^2 \quad (20)$$

with the penalty parameter $\lambda = 1000$ serves as a regularizer and enforces that the weights sum to unity and the DMN is consistent w.r.t. the given volume fraction f , i.e., the equations

$$\sum_{i=1}^{2^K} w_{K+1}^i = 1, \quad \sum_{i=1}^{2^{K-1}} w_{K+1}^{2i} = f \quad \text{and} \quad \sum_{i=1}^{2^{K-1}} w_{K+1}^{2i-1} = 1 - f \quad (21)$$

hold. To assess the accuracy of the fit, we define the sample-wise mean training $e_{\text{mean}}^{\text{train}}$ and validation $e_{\text{mean}}^{\text{valid}}$ error via

$$e_{\text{mean}} = \sum_{s=1}^{N_s} \frac{\|\mathcal{DMN}_Y^{\mathcal{L}}(\mathbb{C}_1^s, \mathbb{C}_2^s, \vec{\mathbf{p}}(f^s, a^s)) - \bar{\mathbb{C}}^s\|_1}{\|\bar{\mathbb{C}}^s\|_1}, \quad (22)$$

where N_s denotes the number of elements in the training and validation sets, respectively. To significantly reduce the number of training epochs and to improve the results in the nonlinear regime, we employ an early-stopping technique as proposed by Dey et al. [128]. For this purpose, we use the identified material parameters of the UPPH matrix and the bundles summarized in Section 3.3 and simulate three unidirectional strain loadings [129]

$$\boldsymbol{\varepsilon} = \varepsilon \mathbf{d} \otimes \mathbf{d} \quad \text{for} \quad \mathbf{d} \hat{=} [\cos(\alpha), \sin(\alpha), 0] \in S^2 \quad \text{and} \quad \alpha \in \{0^\circ, 45^\circ, 90^\circ\} \quad (23)$$

with a strain amplitude of $\varepsilon = 4\%$ for each of the 41 generated SMC microstructures. We consider this generated nonlinear data as the basis of the employed early-stopping technique. To quantify the deviation, we compute the nonlinear mean and maximum validation errors via

$$\eta_{\text{mean}} = \max_{s \in \{1, \dots, N_s\}} \frac{1}{T} \int_0^T \eta_s(t) dt \quad \text{and} \quad \eta_{\text{max}} = \max_{s \in \{1, \dots, N_s\}} \max_{t \in [0, T]} \eta_s(t) \quad \text{with} \quad \eta_s(t) = \frac{\|\bar{\boldsymbol{\sigma}}_s^{\text{DMN}}(t) - \bar{\boldsymbol{\sigma}}_s^{\text{FFT}}(t)\|_1}{\max_{\tilde{t} \in [0, T]} \|\bar{\boldsymbol{\sigma}}_s^{\text{FFT}}(\tilde{t})\|_1} \quad (24)$$

and track them every five epochs. In Figure 6 the training progress is shown. The stepwise reduction of the loss function observed in Figure 6a results from the used learning rate modulation which reduces the learning rate by a factor of two for every 100 epochs starting from an initial learning rate of $\alpha_{\text{ini}} = 1.5 \cdot 10^{-2}$. A closer look at the elastic training $e_{\text{mean}}^{\text{train}}$ and validation $e_{\text{mean}}^{\text{valid}}$ errors in Figure 6b shows that there is no significant model overfitting

| $e_{\text{mean}}^{\text{train}}$ | $e_{\text{mean}}^{\text{valid}}$ | $\eta_{\text{mean}}^{\text{valid}}$ | $\eta_{\text{max}}^{\text{valid}}$ | $\eta_{\text{mean}}^{\text{test}}$ | $\eta_{\text{max}}^{\text{test}}$ |
|----------------------------------|----------------------------------|-------------------------------------|------------------------------------|------------------------------------|-----------------------------------|
| 1.35 % | 1.60 % | 1.90 % | 4.32 % | 2.20 % | 4.71 % |

Table 2: Model performance after training

w.r.t. the linear elastic training data. However, the maximum validation error $\eta_{\text{max}}^{\text{valid}}$ takes its minimum of 4.32 % at 190 epochs and increases thereafter. The early-stopping approach stops the training after another 300 epochs as the nonlinear errors have not improved for the subsequent 60 steps. The best model (at 190 epochs) is then stored.

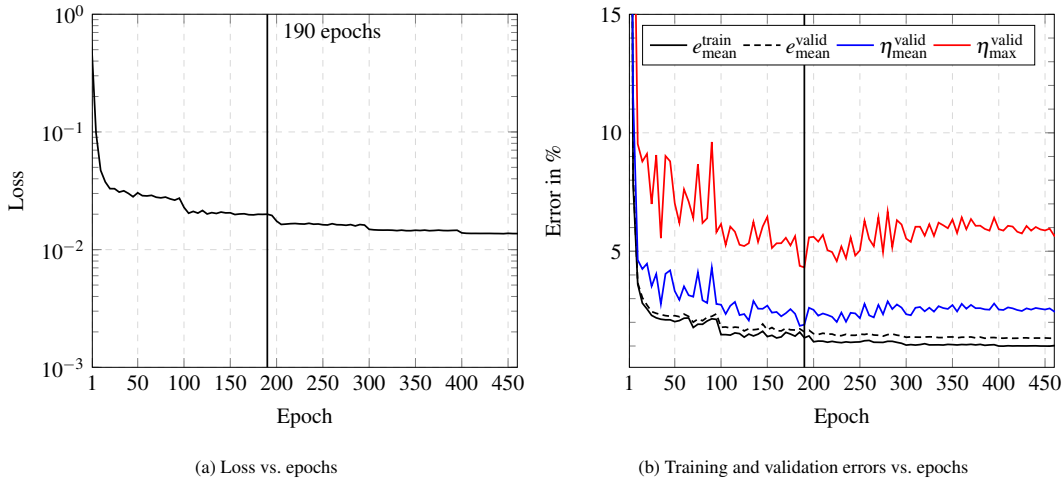


Figure 6: Loss function (a) and model performance during training (b)

To ensure that the DMN generalizes well for all tuples $(f, a) \in [0.15, 0.35] \times [0.5, 0.8]$, we evaluate the DMN on an additional test set, i.e., microstructures the DMN has not seen before. To be more precise, for each black point in Figure 5, i.e., 104 microstructures in total, we generate an artificial SMC microstructure, perform three virtual uniaxial extension tests each (compare equation (23)), and compute the corresponding nonlinear mean and maximum test errors (24). The results are summarized in Table 2. The nonlinear errors evaluated on the test set are only slightly increased compared to the training set. The maximum nonlinear test error (as well as the nonlinear validation error) are well below 5 %, i.e., in the range of engineering requirements, for all considered fiber volume fractions and fiber orientations. Further information on the model validation can be found in Appendix C and the computational setup and the computational costs are presented in Appendix E.2.

3.5. Structural simulation

Each compression molding simulation result is transferred to multiple FE simulation models with fiber orientation and fiber volume fraction data. To be more precise, all 16 mechanical specimens shown in Figure 3 are meshed with *C3D8* Abaqus elements with 3 mm edge length and we apply the procedure described in

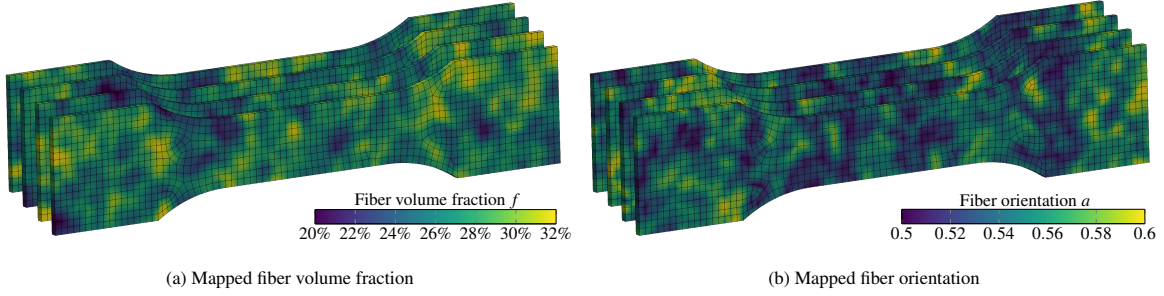


Figure 7: Fiber volume fraction (left) and fiber orientation (right) property fields for different realizations at the same specimen position with identical nominal properties

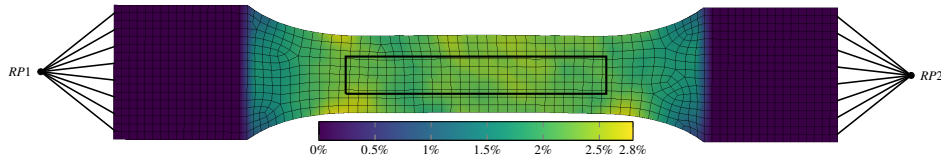


Figure 8: Distribution of the strain ε_{11} component as a result of the applied load in conjunction with the gauge used for averaging the strain

Section 2.2 to virtually cut specimens from the plates. We set the element-wise material orientations to the eigensystem of \mathbf{A} , which reduces the necessary field information to f and a . These fields are interpolated to the nodes of the structural mesh and serve as a predefined field for the subsequent structural simulations (see Figure 7 for an illustration of the mapped data). Contrary to physical plates, we may rotate the virtual plates, virtually cut the specimens and map the aforementioned data. Thus, we generate 1024 unique FE models (64 per plate) with individual distributed property fields. Figure 7 shows several realizations generated in the described way for the specimen shape B2 extracted at identical specimen positions (compare Figure 3). Indeed, as observed in Figure 7, the mold filling simulation predicts highly fluctuating fiber volume fractions and fiber orientations even for identical nominal properties f_0 and a_0 .

For the structural simulations, a unidirectional elongation of 3 mm is applied via the two reference points RP1 and RP2, which are coupled to the specimen arms, see Figure 8. In every Gauss point, a direct DMN is integrated implicitly to incorporate the fiber volume fraction and fiber orientation into the structural simulation.

For the strain measurement, we follow the experimental setup as described in Section 3.1 and record the strain via averaging over the shown gauge section with dimensions $70 \text{ mm} \times 10 \text{ mm}$. The stress is computed by tracking the reaction force at RP2 which is averaged over the cross section. As SMC composites are dominated by brittle failure [25], it suffices to predict crack initiation in order to determine the global failure of the specimen. For this purpose, we assume that crack initiation only occurs in the UPPH matrix. We determine crack initiation when the phase mean of the damage variable q_M describing the isotropic matrix damage exceeds a threshold, i.e., $\langle q_M \rangle_M > 1.3 \%$, in any element of the macroscopic simulation. This threshold is calibrated based on Trauth's [25] experimental results. The stress at crack initiation represents the strength and the correspond-

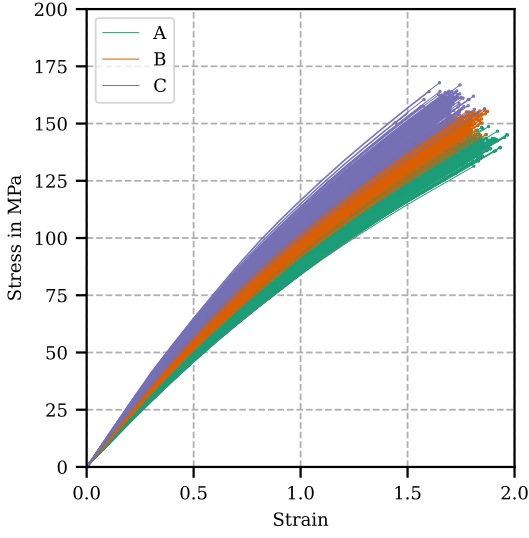


Figure 9: Stress strain curves of all virtual specimens (B1, B2, R1, R2) in configuration A ($f = 22.5\%$), configuration B ($f = 26.0\%$) and configuration C ($f = 29.0\%$) with planar isotropic initial stacks

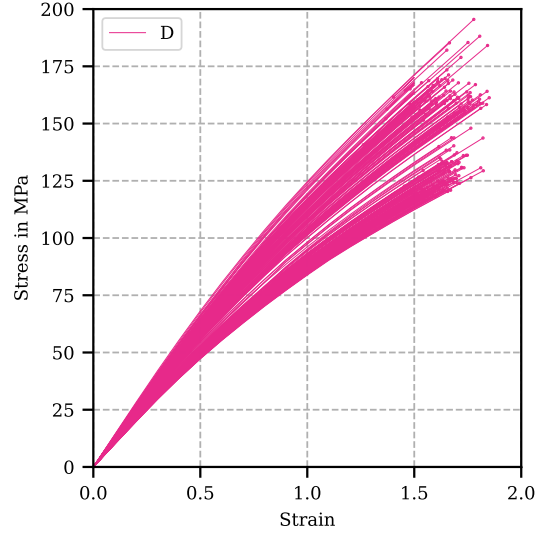


Figure 10: Stress strain curves of all virtual specimens (B1, B2, R1, R2) in configuration D ($f = 26.0\%$) with an initial stack that has an orientation preference ($a_0 = 0.6$). There are two branches for specimens with preferred orientation in load direction and transverse to the load direction

ing strain is the failure strain. The resulting stress-strain curves of all individual virtual specimens (types B1, B2, R1 and R2) are shown in Figure 9 and Figure 10 and saved in a database for further analysis.

4. Uncertainty evaluation, validation and discussion

4.1. Probabilistic evaluation of the virtual process chain

Due to the different initial microstructures resulting from variations in the impregnation process and its propagation through molding, each specimen has different property fields, i.e., fiber volume fraction and fiber orientation, that affect its behavior under loading. Figure 11 outlays a probabilistic virtual process chain that interprets the multitude of specimen realizations as a Gaussian process. Hence, we assume the uncertainty to follow a multivariate Gaussian distribution $\vec{x} \sim \mathcal{N}(\vec{\mu}, \Sigma)$ for a random variable \vec{x} with a probability density distribution $p : \mathbb{R}^k \rightarrow \mathbb{R}$ defined as

$$p(\vec{x}) = \frac{1}{\sqrt{(2\pi)^k \det(\Sigma)}} \exp\left(-\frac{1}{2}(\vec{x} - \vec{\mu})^\top \Sigma^{-1}(\vec{x} - \vec{\mu})\right), \quad (25)$$

where k is the dimensionality of the random variable \vec{x} (see Section 4.4 for a discussion on the applicability of a Gaussian distribution). The mean and the positive semi-definite covariance matrix of \vec{x} are denoted as $\vec{\mu} \in \mathbb{R}^k$ and $\Sigma \in \mathbb{R}^{k \times k}$. The nominal initial state of a stack is given by an initial state vector $\vec{s}_0 = [f_0, a_0]$.

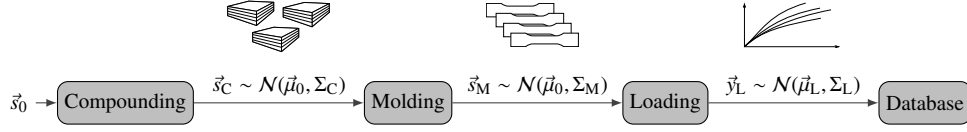


Figure 11: Schematic representation of the probabilistic virtual process chain. The nominal fiber bundle configuration state $\vec{s}_0 = [f_0, a_0]$ is prescribed, while the state after compounding \vec{s}_C and after molding \vec{s}_M follows multivariate Gaussian distributions. Finally, the mechanical behavior including damage is also described by a feature vector \vec{y}_L that follows a multivariate Gaussian distribution.

Compounding. The compounding process introduces uncertainty to the SMC prepreg stacks, as stacks consist of sheets from different sections of the prepreg coil. Properties along this coil may vary due to a preferred fiber orientation or varying fiber volume fraction during production.

For the compounding process, the distribution is given by $\mathcal{N}(\vec{\mu}_0, \Sigma_C)$ assuming that the production process has a mean fulfilling the nominal requirement ($\vec{\mu}_0 = \vec{s}_0$) and a covariance matrix $\Sigma_C \in \mathbb{R}^{2 \times 2}$. The covariance $\Sigma_C = \text{diag}(\sigma_{C,f}^2, \sigma_{C,a}^2)$ is a machine-specific parameter set and we assume no correlation between the state variables as there are no off-diagonal terms in the covariance matrix Σ_C .

Molding. We assume that both, compression molding process and the extraction of specimens, increase the uncertainty, whereas the mean remains unchanged. This assumption is specific to the symmetric centered plate molding application considered here and simplifies the evaluation. By linearity of expectation, the covariance can then be written as

$$\Sigma_M = \text{diag}(\sigma_{C,f}^2 + \sigma_{M,f}^2, \sigma_{C,a}^2 + \sigma_{M,a}^2), \quad \Sigma_M \in \mathbb{R}^{2 \times 2}, \quad (26)$$

where $\sigma_{M,f}$ and $\sigma_{M,a}$ are the additional standard deviations introduced by molding and extraction for fiber volume fraction and orientation, respectively. The values of these parameters depend on the geometry and the molding process parameters. We will estimate these parameters from multiple realizations of the virtual process chain in Section 4.2.

Loading. Finally, the uncertainty of the average state in specimens $\vec{s}_M \in \mathbb{R}^2$ translates to uncertainties of the features upon loading $\vec{y}_L \in \mathbb{R}^N$. The feature vector $\vec{y}_L \in \mathbb{R}^N$ may contain N loading features such as Young's modulus, strength or stresses at specific strains imposed to the specimens. For a linear combination

$$\vec{y}_L = M \vec{s}_M \quad (27)$$

with $M \in \mathbb{R}^{N \times 2}$, we may compute the covariance matrix of the N loading features by linear propagation of uncertainty

$$\Sigma_L = M \Sigma_M M^T. \quad (28)$$

Similar to $\sigma_{M,f}$ and $\sigma_{M,a}$, the feature-extraction matrix M depends on the geometry and material. It is also estimated from multiple evaluations of the virtual process chain in Section 4.3.

4.2. The effect of size on uncertainty

First, we verify that the predicted fiber configuration accurately predicts scatter of fiber volume fraction across the plates. Figure 12 summarizes the evaluation of all 15 round TGA samples for each realization. The standard deviation of fiber volume fraction within a plate $\hat{\sigma}_f$ ranges from 1.10 % to 1.59 % in the simulation models. This is in good agreement with the experimental data obtained by Trauth [25] which ranges from 0.91 % to 2.38 %. However, the experiments also feature scatter between individual plates. Assuming that the mean fiber volume content of each plate is representative for a plate, we estimate the standard deviation of the compounding machine to be $\sigma_{C,f} = 1.40$ %.

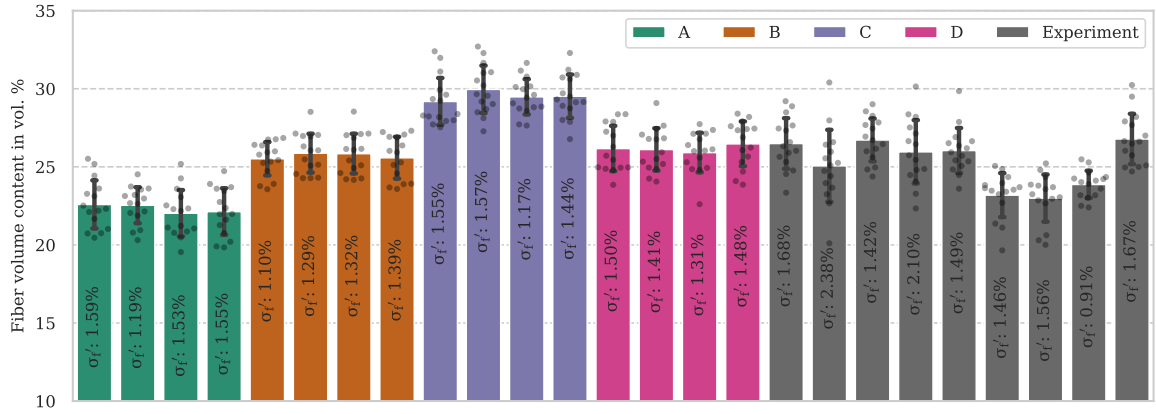


Figure 12: Simulated fiber volume fraction evaluated at TGA specimen positions and experimentally evaluated TGA specimens by Trauth [25] (gray)

The uncertainty also depends on the specimen size, as larger specimens tend to average over larger fractions of the fiber configuration. We describe the specimen size by a characteristic length L , which is computed as $L = V^{1/3}$ from the specimen volume V . We presume that the standard deviation of fiber volume fraction $\sigma_{M,f}$ and of orientation preference $\sigma_{M,a}$ after molding are roughly inversely proportional to the characteristic specimen size. More precisely, we presume an L^{-1} scaling of the standard deviations, which is typical for processes with non-negligible boundary-layer errors (cutting specimens from the plates), see, e.g., Schneider [130]. A linear approximation is given by

$$\sigma_{M,f}(L) \approx \frac{1\%}{0.058 \text{ mm}^{-1}L} \quad \text{and} \quad \sigma_{M,a}(L) \approx \frac{1}{4.184 \text{ mm}^{-1}L}, \quad (29)$$

which is obtained from the standard deviation of differently sized regions evaluated on the full plate (see Figure F.19 in Appendix F). The regions are obtained by evaluating the fiber configuration on a full plate with dimensions $400 \text{ mm} \times 400 \text{ mm} \times 3 \text{ mm}$, which is meshed with 3 mm edge length. The different sizes are then realized by grouping elements to square-shaped subsets of different sizes.

The approximations provide a simple estimate for the intrinsic uncertainty of properties after plate molding.

Even for a perfectly controlled process with absolutely identical material parameters of all constituents, we will observe this level of uncertainty due to the random microstructure and location.

4.3. Contributions to uncertain mechanical properties

To evaluate the propagation of uncertain processing effects to mechanical loading, we define a feature vector $\vec{y}_L \in \mathbb{R}^{18}$ containing Young's modulus, strength, failure strain and stresses from 0.1 % to 1.5 % with a stepsize of 0.1 %. Using all realizations of the virtual process chain \mathcal{Y} , we minimize the component-wise squared residuals

$$\sum_{i \in \mathcal{Y}} (M \vec{s}_{M,i} - \vec{y}_{L,i})^2 \rightarrow \min_M \quad (30)$$

to obtain the feature-extraction matrix M . With this strategy, we compute the covariance matrix of the loading curve Σ_L for the following three different cases of covariance matrices for the molded state Σ_M using equation (28):

Base A perfect compounding process and perfect molding process with uncertainty only originating from different microstructure realizations

$$\Sigma_M^{\text{Base}} = \text{diag}(\sigma_{M,f}^2(L), \sigma_{M,a}^2(L)) \quad (31)$$

FVF A compounding process with a standard deviation of $\sigma_{C,f} = 1.40\%$ for the fiber volume fraction (FVF) in stacks

$$\Sigma_M^{\text{FVF}} = \text{diag}(\sigma_{C,f}^2 + \sigma_{M,f}^2(L), \sigma_{M,a}^2(L)) \quad (32)$$

FVF+ORI A compounding process with an additional standard deviation $\sigma_{C,a} = 0.05$ of the orientation state (ORI) in stacks

$$\Sigma_M^{\text{FVF+ORI}} = \text{diag}(\sigma_{C,f}^2 + \sigma_{M,f}^2(L), \sigma_{C,a}^2 + \sigma_{M,a}^2(L)) \quad (33)$$

Evaluating a multitude of realizations of the virtual process permits us to estimate uncertainties associated to the loading curves of specimens from SMC plates. Subsequently, we simulate loading of a single homogeneous specimen and add an uncertainty estimation. Figure 13 illustrates results of this procedure with colored areas indicating the $\pm 3\sigma$ confidence interval containing approximately 99 % of all realizations for the four specimen types (R1, R2, B1, B2) investigated here. The base uncertainty (brown in Figure 13) is slightly larger for the smaller specimen type R1 with 15 mm width in the loading area. This contribution accounts only for a fraction of the total uncertainty observed in experiments (gray with error bars indicating a $\pm 3\sigma$ confidence interval in Figure 13). Accounting for a variance of the fiber volume fraction between stacks results in an increase of predicted uncertainty (the area displayed in yellow in Figure 13) with a contribution similar to the basic microstructure-induced uncertainty. Small deviations of orientation in the stack propagate significantly through the molding process and mechanical loading, such that a deviation of $\sigma_{C,a} = 0.05$ could explain the entire remaining contribution matching experimental error bars.

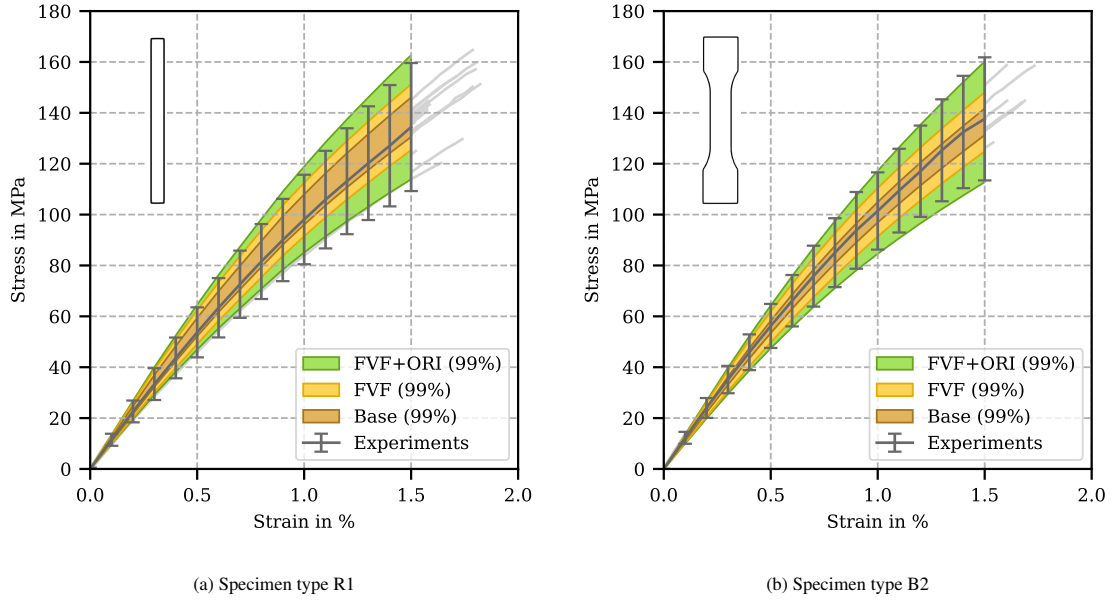


Figure 13: Stress-strain relations for the smallest and largest specimens

Additionally, evaluating the probabilistic virtual process chain allows to estimate the error propagation affecting strength, failure strain and Young's modulus including their correlation. Figure 14 shows experimental results for strength and Young's modulus obtained by Trauth [25] as gray points.

The simulation results for 22.5 %, 26 % and 29 % nominal fiber volume fraction (configurations A, B and C) are shown as green, orange and purple points, respectively. The position of these clusters indicates an increase of strength and Young's modulus with increasing nominal fiber volume fraction. The simulation results for 26 % nominal fiber volume fraction and an orientation preference $a_0 = 0.6$ (configuration D) results in two separate clusters illustrated by pink points separating those specimens tested in preferred fiber direction and those transverse to the preferred direction. The increase of strength and Young's modulus with increasing fiber orientation follows a different relation than the one with changing fiber volume fraction. For a preferred fiber orientation in loading direction, fibers carry more load and fatal matrix damage occurs at higher stress levels compared to a specimen without orientation preference that has the same initial Young's modulus due to a higher fiber volume fraction.

The 99 % confidence interval for the contribution for the *Base* case (brown ellipse), the *FVC* case (yellow ellipse) and the *FVC+ORI* case (green ellipse) are also shown in Figure 14. Even though the covariance of the molding state Σ_M is uncorrelated, the propagation to the covariance of the loading curve Σ_L includes the correlation and rotates the ellipses if the ratio of variance due to fiber volume fraction and orientation changes. Evaluating the basic uncertainty recovers simulation results with nominal stack properties. Adding the variance of fiber volume fraction between stacks to the model stretches the ellipse such that its first principal axis aligns

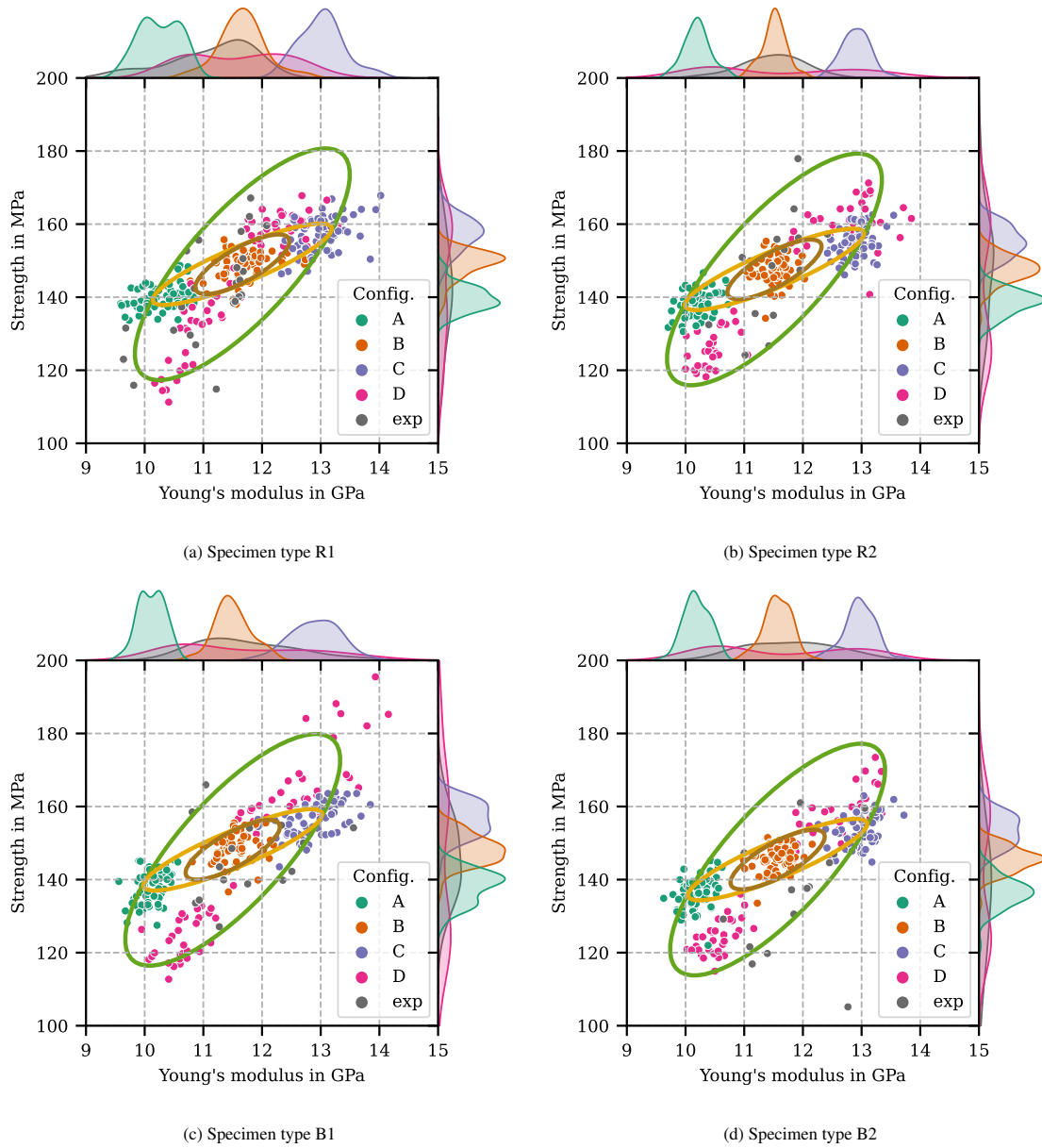


Figure 14: Correlations between strength and Young's modulus for simulated cases (colored points), experiments (gray points) and estimations of 99% confidence intervals (ellipses).

with the simulated clusters for different fiber volume fractions (yellow in Figure 14). Adding additional uncertainty from the orientation rotates the ellipse to align with the clusters from different preferred orientation states and increases the uncertain domain significantly. The experimental results are predominantly located within this ellipse, however isolated points are found further away. These are likely influenced by uncertainties outside the scope of this model, such as crack initiation during specimen clamping.

4.4. Discussion of model simplifications

In this work, we focus on planar fiber orientation distributions and thus simplify the parametrization of the orientation state to a single variable a . This is reasonable, as the out-of-plane component never exceeds a value of $A_{zz} = 1.5\%$ in our application. However, advanced structural SMC applications often deviate from the planar state. The proposed procedure could be enhanced for such cases with an advanced generator for three-dimensional SMC bundle structures as well as an extension of the orientation parametrization and interpolation scheme.

The proposed inverse relation of standard deviation and characteristic length of specimens is a rough estimation without any claim of general validity. The standard deviation plotted in Figure F.19 is an average value influenced by a location effect.

The uncertainty evaluation models property distributions as multivariate Gaussians. However, the properties are limited to a certain domain (e.g. fiber volume fraction $f \in [0, 1]$) and the Gaussian probability distribution would predict a small probability outside the admissible domain. This could be addressed with truncated Gaussian distributions, but in the application here, the probability outside the admissible range is so marginal, that we prefer regular Gaussians for simplicity.

The machine specific orientation uncertainty in compounded stacks is only estimated and not measured. The value could be smaller, thus leaving the remaining uncertainty of experimental results to other effects such as varying material properties or crack initiation upon clamping to name a few. These additional uncertainties may also be the reason why some experimental results in Figure 14 are located outside the predicted confidence ellipses.

5. Conclusions and outlook

The developed virtual process chain for SMC is a complete digital representation of specimen lives from prepreg manufacturing to failure upon testing. The applied direct process simulation computes outcomes of an SMC compression molding process with different initial realizations of a fiber bundle stack. Virtual specimens with individual fields for fiber orientation and fiber volume fraction are informed with these molding results for structural simulation. The structural macroscale simulation is based on a multiscale damage model, which is upscaled via a micro-oriented deep material network using appropriate interpolation techniques. The resulting database of virtual samples is evaluated with a Gaussian process model and compared to experimental results.

There is an inherent size dependent base uncertainty, which can be quantified approximately by a inverse proportional relation to the characteristic length. This base uncertainty cannot be improved by more accurate processing, more careful testing or more samples - it is intrinsic to this type of composite. Additional uncertainty is introduced by propagation of uncertainties from the SMC prepreg stack. This propagated uncertainty represents a significant contribution to the total uncertainty associated with the investigated SMC specimens. Characterizing the fiber orientation and fiber volume fraction during SMC prepreg production is an interesting field for future work due to its significant contribution to uncertainty. Manufacturers of SMC stacks may reduce the uncertainty by shuffling sheets in a stack in such a way that the variance is minimized.

The work at hand demonstrates that it is imperative to have powerful upscaling techniques available in order to conduct two-scale simulations of microstructured materials. We show that it is essential to consider the locally varying microstructure characteristics in a macroscopic simulation in order to capture the probabilistic process chain with good accuracy. The outstanding efficiency, the high fidelity and reliability and the possibility of extension by interpolation schemes make direct DMN a powerful piece of technology for multiscale simulations. The coupled evaluations are not limited to the simple specimens shown here. The proposed simulation framework can be applied to entire parts by automated computation of multiple virtual realizations. Quantifying the uncertainty of such parts leverages the full light weighting potential by omitting over-dimensioned structures that account for uncertainty by rough safety factors.

Acknowledgements

NM, SG and JG thank M. Bartkowiak and A. Trauth for providing detailed insight into their experimental procedures, observations and knowledge regarding our considered SMC specimens. The research documented in this manuscript has been funded by the Deutsche Forschungsgemeinschaft (DFG, German Research Foundation), project number 255730231, within the International Research Training Group “Integrated engineering of continuous-discontinuous long fiber reinforced polymer structures“ (GRK 2078). The work also benefited from discussion with DFG project MeproSi, project number 464119659, which aims at a probabilistic CAE chain for injection molded parts, considering uncertainties in microstructure, process conditions and material properties. The support by the German Research Foundation (DFG) is gratefully acknowledged.

Declaration of competing interest

The authors declare that they have no known competing financial interests or personal relationships that could have appeared to influence the work reported in this publication.

CRedit authorship contribution statement

NM, SG, JG, LK and TB were responsible for the development of the methodology presented in this publication. NM, AH, LK, and FH developed the direct bundle compression molding approach. SG, MS and TB established the deep material network. JG, MS, AH and TB developed the anisotropic damage model. Conceptualization and establishment of the probabilistic process chain was taken over by NM, SG and JG. Validation, investigation of the results, formal analysis and the subsequent visualization were performed by NM, SG and JG. Resources were provided by LK, FH, MS and TB. The original manuscript draft was written by NM, SG and JG and extensively reviewed and edited by all authors. The research project was administrated by NM, SG and JG. Funding was acquired by LK, MS, FH and TB. The research was supervised by LK, MS, AH, FH and TB.

Appendix A. Generation of initial SMC stack

The direct bundle simulation requires to generate fiber bundles in the initial stack that represent the initial fiber bundle configuration before molding. To draw and place the bundles we follow the procedure presented by Görthofer et al. [18]. The corresponding placement procedure for a single bundle is illustrated in Figure A.15 and is repeated until the total fiber volume fraction equals the prescribed SMC fiber volume fraction.

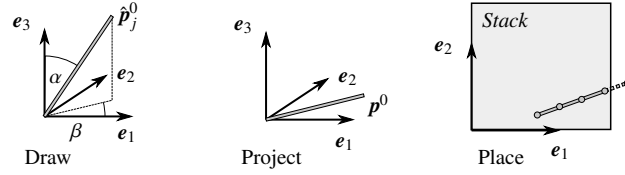


Figure A.15: Illustration of a single bundle generation in the initial SMC stack

To place a single bundle in the initial stack, we draw a primer direction according to

$$\hat{\boldsymbol{p}}^0 = \sin(\alpha) \cos(\beta) \boldsymbol{e}_1 + \sin(\alpha) \sin(\beta) \boldsymbol{e}_2 + \cos(\alpha) \boldsymbol{e}_3, \quad (\text{A.1})$$

where $\alpha \in \mathcal{U}(-1, 1)$ and $\beta \in \mathcal{U}(0, 2\pi)$ where $\mathcal{U}(a, b)$ denotes a uniform probability distribution on the interval $[a, b]$. Then, we map this primer direction to a prescribed initial planar fiber orientation state \boldsymbol{A}^0 by

$$\boldsymbol{p}^0 = \boldsymbol{A}^0 \hat{\boldsymbol{p}}^0 \quad (\text{A.2})$$

and normalize it to unity. We generate a fiber bundle comprised of several one dimensional elements with this direction and randomly translate it within the rectangular domain of the initial stack by a shift vector $\Delta \boldsymbol{x} \in \mathcal{U}(\Delta \boldsymbol{x}_{\min}, \Delta \boldsymbol{x}_{\max})$, where $\Delta \boldsymbol{x}_{\min}$ and $\Delta \boldsymbol{x}_{\max}$ denote the minimum and maximum allowed shifts such that at least one node of the bundle resides within the initial stack domain. All elements outside the initial stack are deleted, such that bundles close to the edge of the stack are shorter. This introduces a length distribution of bundles with 12 % of fiber bundles being shorter than the nominal length of 25 mm in the investigated application here. The fiber bundles may overlap each other initially, which is either resolved by adjusting node positions in an initial overlap adjustment or, if that is not possible, by storing the offsets for contacts between bundles and resolving it during the flow process. The procedure yields fiber bundles following a central Gaussian distribution [131] that captures the sought orientation state to high accuracy [18].

Appendix B. Efficient implementation of micro-oriented direct deep material networks

For a detailed summary of the implementation as a user-defined subroutine, we refer to Gajek et al. [22] for the purely mechanical and to Gajek et al. [24] for the thermomechanical case. Please note that the mere

difference in implementation between the work at hand and the aforementioned works is the additional rotation layer which rotates the computed stresses and strains (and algorithmic tangents) of the materials.

We assume that the parameter vector \vec{p} is given as the result of a suitable interpolation scheme $(f, a) \mapsto \vec{p}(f, a)$ and fixed. First, we introduce the averaging operator $\mathbf{B} : \text{Sym}(3)^{2^K} \rightarrow \text{Sym}(3)$, a 2^K -fold copy of the identity on $\text{Sym}(3)$ and the symmetrized gradient operator $\mathbf{D} : (\mathbb{R}^3)^{2^K-1} \rightarrow \text{Sym}(3)^{2^K}$, which depends on the vector of lamination directions \vec{n} and the vector of weights \vec{w} and which encodes the DMN's topology into a single linear mapping, see Gajek et al. [21] or Dey et al. [128] for the specific structure of the gradient operator \mathbf{D} . Then, the vector of compatible strains $\vec{\varepsilon} \in \text{Sym}(3)^{2^K}$ of the DMN admits the representation

$$\vec{\varepsilon} = \mathbf{B}^T \bar{\varepsilon} + \mathbf{D} \vec{u} \quad (\text{B.1})$$

where $\bar{\varepsilon} \in \text{Sym}(3)$ designates the macrostrain (increment) and $\vec{u} \in (\mathbb{R}^3)^{(2^K-1)}$ stands for the vector of (unknown) displacements. Next, we define the vector of incremental algorithmic potentials $\vec{\Psi} = [\Psi_1, \dots, \Psi_{2^K}]$, alternating between the incremental potentials of both phases, i.e.,

$$\Psi_i = \begin{cases} \Psi_1, & i \text{ odd,} \\ \Psi_2, & i \text{ even,} \end{cases} \quad (\text{B.2})$$

see Gajek et al. [21, 22, 24] for more information. The incremental algorithmic potential $\Psi_i : \text{Sym}(3) \times \mathcal{Z}_i \rightarrow \mathbb{R}$ of the i -th phase is the result of a time discretization by the implicit Euler method

$$\Psi_i(\varepsilon, z_i^n) = \inf_{z_i^{n+1} \in \mathcal{Z}_i} \left(\psi_i(\varepsilon, z_i^{n+1}) + \Delta t \phi_i \left(\frac{z_i^{n+1} - z_i^n}{\Delta t} \right) \right), \quad (\text{B.3})$$

where z_i^n designates the internal variables of the last converged time step. The microscopic vector of stresses is defined via

$$\vec{\sigma}(\vec{\varepsilon}, \vec{z}^n) = \vec{\mathbf{R}}^{-1} \star \frac{\partial \vec{\Psi}}{\partial \vec{\varepsilon}}(\mathbf{R} \star \vec{\varepsilon}, \vec{z}^n) \quad \text{with} \quad \frac{\partial \vec{\Psi}}{\partial \vec{\varepsilon}}(\cdot, \vec{z}^n) = \left[\frac{\partial \Psi_1}{\partial \vec{\varepsilon}}(\cdot, z_1^n), \dots, \frac{\partial \Psi_{2^K}}{\partial \vec{\varepsilon}}(\cdot, z_{2^K}^n) \right], \quad (\text{B.4})$$

where $\vec{z}^n = [z_1, \dots, z_{2^K}] \in \vec{\mathcal{Z}}$ denotes the vector of internal variables and the operator $\vec{\mathbf{R}} \star : \text{Sym}(3)^{2^K} \rightarrow \text{Sym}(3)^{2^K}$ encodes a forward rotation of strains

$$\vec{\varepsilon} \mapsto \vec{\mathbf{R}} \star \vec{\varepsilon} = [\mathbf{R}_1^T \varepsilon_1 \mathbf{R}_1, \dots, \mathbf{R}_{2^K}^T \varepsilon_{2^K} \mathbf{R}_{2^K}] \quad (\text{B.5})$$

and $\vec{\mathbf{R}}^{-1} \star : \text{Sym}(3)^{2^K} \rightarrow \text{Sym}(3)^{2^K}$ denotes the corresponding backward rotation of stresses

$$\vec{\sigma} \mapsto \vec{\mathbf{R}}^{-1} \star \vec{\sigma} = [\mathbf{R}_1 \sigma_1 \mathbf{R}_1^T, \dots, \mathbf{R}_{2^K} \sigma_{2^K} \mathbf{R}_{2^K}^T], \quad (\text{B.6})$$

both expressed in terms of the vector of rotation matrices $\vec{\mathbf{R}} = [\mathbf{R}_1, \dots, \mathbf{R}_{2^K}] \in \mathcal{R}$. Then, for a prescribed total macrostrain increment $\bar{\varepsilon}$, we seek the vector of displacements \vec{u} , which solves the balance of linear momentum

$$\mathbf{D}^T \mathbf{W} \vec{\mathbf{R}}^{-1} \star \frac{\partial \vec{\Psi}}{\partial \vec{\varepsilon}}(\vec{\mathbf{R}} \star (\mathbf{B}^T \bar{\varepsilon} + \mathbf{D} \vec{u}), \vec{z}^n) = \mathbf{0}, \quad (\text{B.7})$$

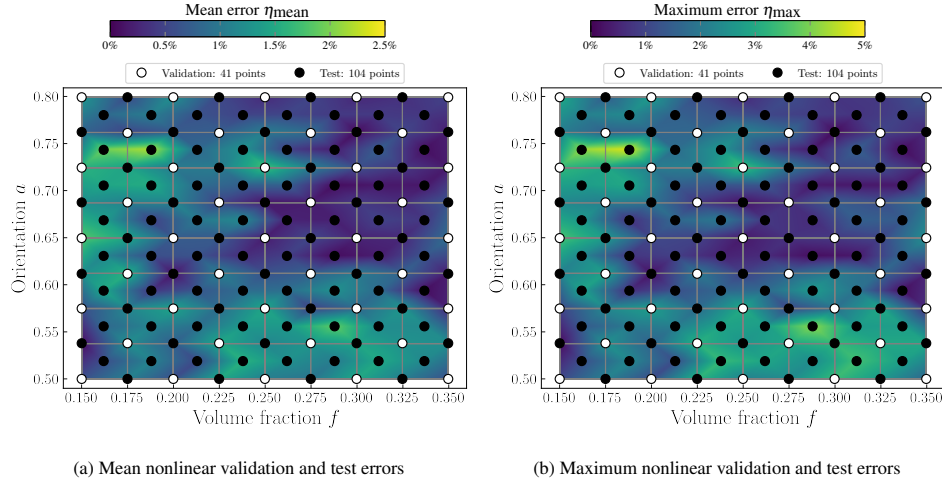


Figure C.16: Distribution of mean and maximum nonlinear validation and test errors on the space of admissible fiber volume fractions and fiber orientations

where $\mathbf{W} \in \text{Sym}(3)^{2^K} \rightarrow \text{Sym}(3)^{2^K}$ designates the weighting matrix, a diagonal matrix comprising the weights \vec{w} for which

$$\mathbf{W} = \text{diag}\left(w_{K+1}^1, \dots, w_{K+1}^{2^K}\right) \quad (\text{B.8})$$

holds. In a subsequent step, the effective stress $\vec{\sigma}$ is computed by averaging the phase stresses via

$$\vec{\sigma} = \mathbf{B}\mathbf{W}\vec{\mathbf{R}}^{-1} \star \vec{\sigma}(\vec{\mathbf{R}} \star (\mathbf{B}^T \vec{\varepsilon} + \mathbf{D}\vec{u}), \vec{z}^n). \quad (\text{B.9})$$

Appendix C. Model validation

To investigate the DMN's approximation capabilities, Figure C.16a and C.16b summarize the mean and maximum errors over the space of admissible fiber volume fractions and fiber orientations. We observe that both errors are strongly correlated, i.e., large mean errors imply large maximum errors and vice versa. Furthermore, both errors fluctuate noticeably without indicating any distinguished dependence on certain fiber volume fractions or fiber orientations. For all considered microstructure realizations, even the ones the DMN was not trained but only interpolated on, the DMN gives nonlinear maximum errors well below 5%.

Figure C.17 gives an impression on how the computed nonlinear errors listed in Table 2 translate into actual stress-strain curves. Illustrated are the predicted effective stress $\vec{\sigma}_{11}$ as well as the nonlinear error η (24) for an uniaxial extension in the 11-direction computed in 40 equidistant time steps and a macroscopic strain of $\vec{\varepsilon} = 4\%$. We report the results for the planar fiber orientation $a = 0.5$ in Figure C.17a as well as for the more aligned cases of $a = 0.65$ and $a = 0.80$ in Figures C.17b and C.17c separately. Furthermore, we vary the fiber volume fraction from $f = 0.15$ to $f = 0.35$ in five equidistant steps.

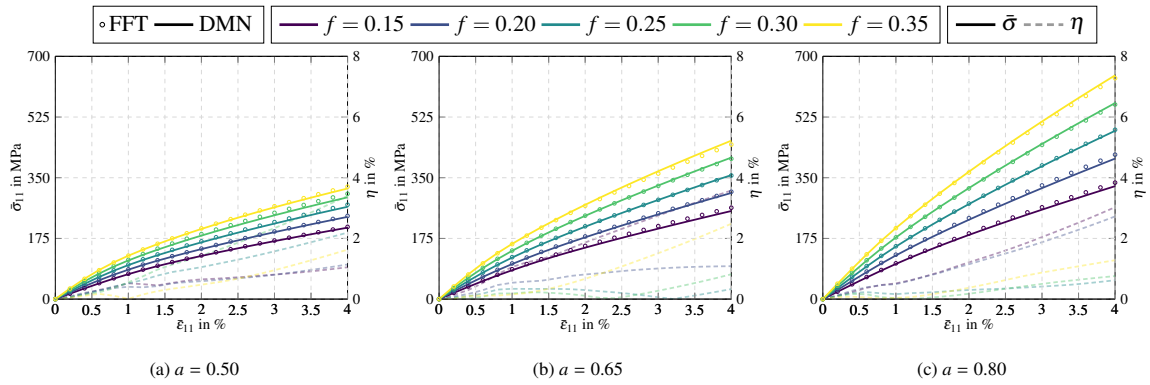


Figure C.17: Comparison of full-field solution and meta model for a variety of fiber orientations and fiber volume fractions

We observe that the predicted effective stresses (in the 11-direction) depends significantly on the fiber volume fraction as well as the fiber orientation. For all considered cases, the DMN gives an excellent prediction with nonlinear errors well below 4 %.

Appendix D. Determination of unit cell properties

Using a modified random sequential adsorption approach [132] with a quasi-random Sobol' ansatz [133] in combination with the exact closure in two dimensions [18], we generate high fidelity unit cells for SMC as introduced by Chen et al. [11] and extended by Görthofer et al. [18]. The inescapable trade-off is the generation of unit cells that are on the one hand as small as possible to minimize the computational effort and on the other hand as large as necessary to ensure representativity. Following a procedure as presented in Görthofer et al. [18] and aiming for a relative error of no more than 2 % for the effective transversely isotropic engineering constants of SMC, we identify appropriate dimensions of the unit cells to be $500 \times 500 \times 50$ voxels that is $12.5 \cdot 10^6$ voxels, see Figure D.18. The indices "L" and "T" of the engineering constants indicate the longitudinal and transverse direction, respectively.

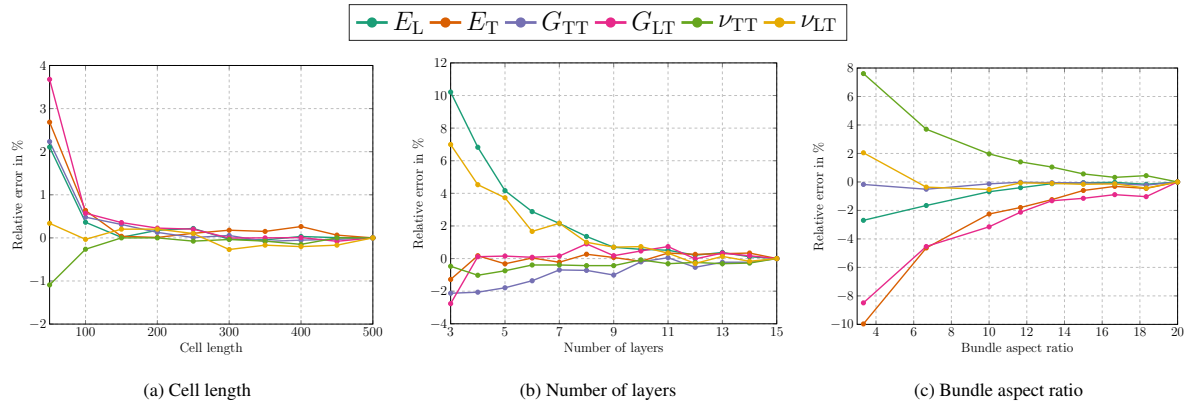


Figure D.18: Determination of unit cell properties based on effective transversely isotropic engineering constants

Appendix E. Computational setups

Appendix E.1. Direct bundle simulation

We ran simulations on 16-core workstations with SIMULIA Abaqus 2021 and custom subroutines VDLLOAD, VEXTERNALDB, VUFIELD, VSDFIELD, VUAMP, VUVISCOSITY compiled with the INTEL ifort 16 compiler. The simulations took 15 h to 30 h wall clock time depending on the number of bundles and the processor. The data mapping described in Section 2.2 is implemented as a ParaView filter (https://github.com/nilsmeyerkit/paraview_map_lines) that requires 30 s to 60 s wall clock time per specimen on a single core depending on specimen size.

Appendix E.2. Structural simulation

The training of the DMN and the two-scale simulations were performed on a workstation equipped with two AMD EPYC 7642 with 48 physical cores each, enabled SMT and 1024 GB of DRAM. Sampling the linear

elastic training data took about 12 h wall clock time where six load steps were computed in parallel on 16 cores each. The training of the DMN took about 3 h wall clock time. Computing all 1024 two-scale simulations took about 10 h, i.e., about 35 s per simulation, with 12 executions in parallel running on 8 cores each.

Appendix F. Size dependency

The approximations in equation (29) are plotted in Figure F.19 in black for comparison to evaluations of the standard deviation between different subsets of the plate for varying subset size.

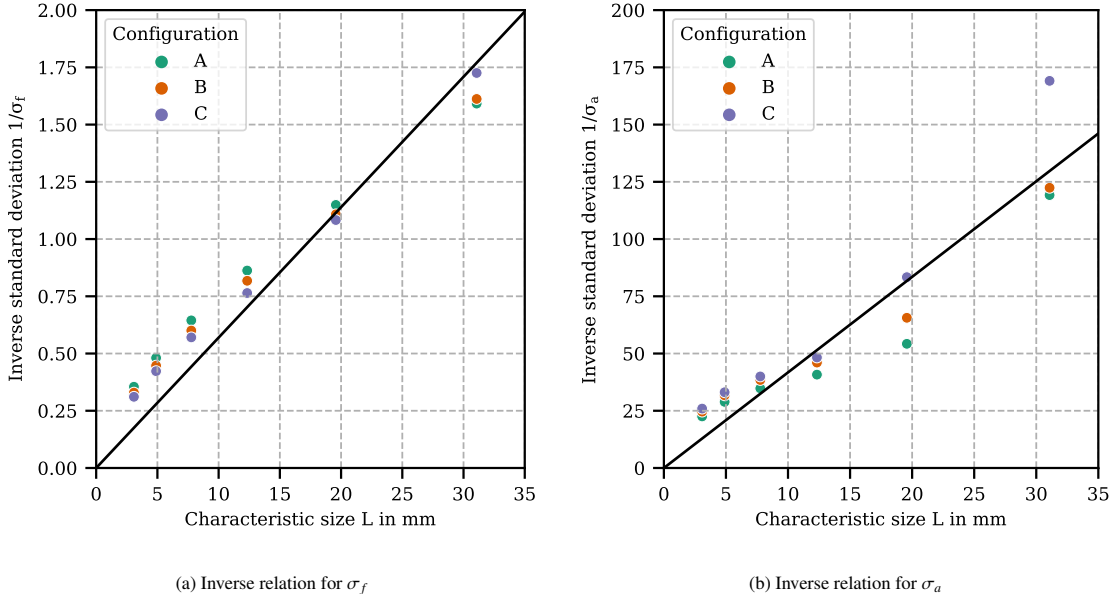


Figure F.19: The scatter is approximately inversely proportional to the characteristic specimen size

Appendix G. Parameters

| Property | Symbol | Value |
|------------------------------------|------------------|---|
| Reference viscosity | D_1 | 72 kPa s |
| Transition shear rate | $\dot{\gamma}_0$ | 0.1 s^{-1} |
| Power-law viscosity coefficient | n | 0.385 |
| Temperature parameter | T^* | 40.73 °C |
| Fitting parameter | A_1 | 7.94 |
| Fitting parameter | A_2 | 105.96 °C |
| Matrix mass density | ρ | 1480 kg m ⁻³ |
| Thermal conductivity | κ | 0.163 W m ⁻¹ K ⁻¹ |
| Gap conductance | k_T | 403 W m ⁻² K ⁻¹ |
| Specific heat capacity | c_p | 1530 J kg ⁻¹ K ⁻¹ |
| Reference velocity | v_0 | 1 mm s ⁻¹ |
| Hydrodynamic power-law coefficient | m | 0.6 |
| Hydrodynamic friction coefficient | λ | 3.0 MN s m ⁻³ |
| Mass scaling factor | | 3×10^5 |
| Bundle cross section | A_B | 0.03 mm ² |
| Maximum compression force | F_{\max} | 6 MN |

Table G.3: Parameters for the direct bundle simulation

| | Young's modulus in GPa | Poisson's ratio | Shear modulus in GPa |
|-------------|------------------------|--------------------|----------------------|
| Fibers [25] | $E_F = 72.00$ | $\nu_F = 0.220$ | $G_F = 29.51$ |
| Matrix [25] | $E_M = 3.45$ | $\nu_M = 0.385$ | $G_M = 1.25$ |
| Bundles | $E_L = 51.48$ | $\nu_{TT} = 0.402$ | $G_{TT} = 6.63$ |
| | $E_T = 18.66$ | $\nu_{LT} = 0.260$ | $G_{LT} = 6.82$ |

Table G.4: Elastic properties of fibers, matrix and bundles

| | Extraction tensor | σ_0 in MPa | H in MPa | m |
|---------|-----------------------------|-------------------|------------|-----|
| Matrix | \mathbb{B}_M Eq. (10) | 36.88 | 213.92 | 1.0 |
| Bundles | $\mathbb{B}_{B,N}$ Eq. (11) | 46.03 | 529.00 | 1.0 |
| | $\mathbb{B}_{B,S}$ Eq. (12) | 44.08 | 283.92 | 1.0 |

Table G.5: Damage parameters for matrix and bundles

Appendix H. Additional plots

In addition to the plots for specimens R1 and B2 in Figure 13, results for specimens R2 and B1 are given in Figure H.20 for completeness.

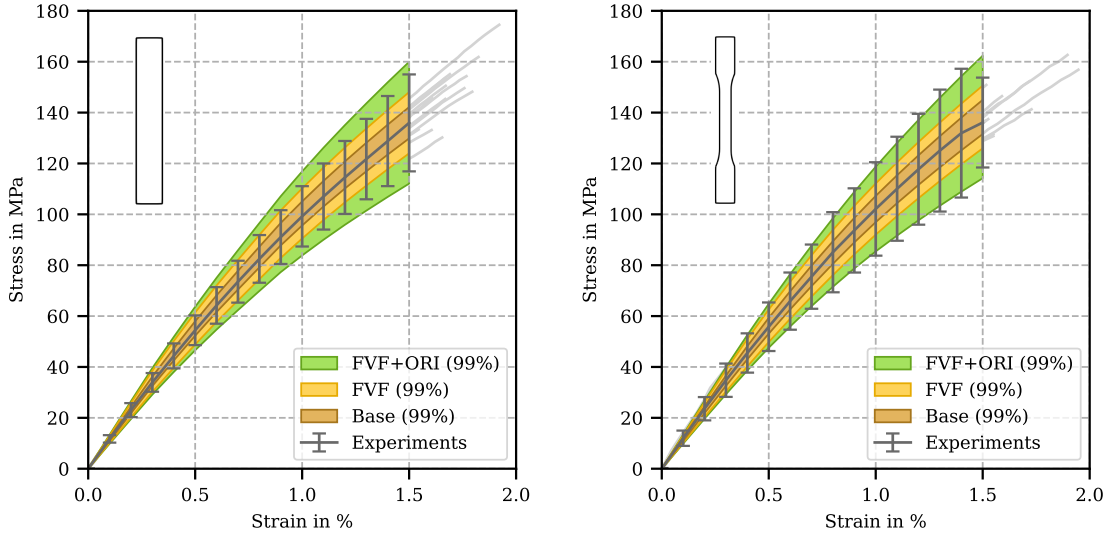


Figure H.20: Stress-strain relations for other specimen types

References

- [1] M. Schemmann, B. Brylka, S. Gajek, T. Böhlke, Parameter Identification by Inverse Modelling of Biaxial Tensile Tests for Discontinuous Fiber Reinforced Polymers, *PAMM* 15 (1) (2015) 355–356.
- [2] M. Schemmann, S. Gajek, T. Böhlke, Biaxial Tensile Tests and Microstructure-Based Inverse Parameter Identification of Inhomogeneous SMC Composites, in: H. Altenbach, F. Jablonski, W. H. Müller, K. Naumenko, P. Schneider (Eds.), *Advances in Mechanics of Materials and Structural Analysis: In Honor of Reinhold Kienzler*, Vol. 80, Springer International Publishing, 2018, pp. 329–342.
- [3] S. G. Advani, C. L. Tucker, The Use of Tensors to Describe and Predict Fiber Orientation in Short Fiber Composites, *Journal of Rheology* 31 (8) (1987) 751–784.
- [4] M. Schneider, An algorithm for generating microstructures of fiber-reinforced composites with long fibers, *International Journal for Numerical Methods in Engineering* (2022).
- [5] L. Kärger, A. Bernath, F. Fritz, S. Galkin, D. Magagnato, A. Oeckerath, A. Schön, F. Henning, Development and validation of a CAE chain for unidirectional fibre reinforced composite components, *Composite Structures* 132 (2015) 350–358.
- [6] F. Buck, B. Brylka, V. Müller, T. Müller, K. A. Weidenmann, A. N. Hrymak, F. Henning, T. Böhlke, Two-scale structural mechanical modeling of long fiber reinforced thermoplastics, *Composites Science and Technology* 117 (2015) 159–167.
- [7] J. Görthofer, N. Meyer, T. D. Pallicity, L. Schöttl, A. Trauth, M. Schemmann, M. Hohberg, P. Pinter, P. Elsner, F. Henning, A. Hrymak, T. Seelig, K. Weidenmann, L. Kärger, T. Böhlke, Virtual process chain of sheet molding compound: Development, validation and perspectives, *Composites Part B: Engineering* 169 (2019) 133–147.
- [8] H. G. Kia, Flow characteristics of sheet molding compound in panels with integrated ribs, *Journal of Reinforced Plastics and Composites* 10 (6) (1991) 626–644.
- [9] L. Bretz, B. Häfner, G. Lanza, Non-destructive measurement of fiber mass content of glass fiber sheet molding compound using Terahertz radiation, *Measurement* 168 (2021) 108386.
- [10] F. Rothenhäusler, N. Meyer, S. Wehler, M. Hohberg, M. Gude, F. Henning, L. Kärger, Experimental and Numerical Analysis of SMC Compression Molding in Confined Regions—A Comparison of Simulation Approaches, *Journal of Composites Science* 6 (3) (2022) 68.
- [11] Z. Chen, T. Huang, Y. Shao, Y. Li, H. Xu, K. Avery, D. Zeng, W. Chen, X. Su, Multiscale finite element modeling of sheet molding compound (SMC) composite structure based on stochastic mesostructure reconstruction, *Composite Structures* 188 (2018) 25–38.

- [12] R. Mansour, A. Kulachenko, W. Chen, M. Olsson, Stochastic constitutive model of isotropic thin fiber networks based on stochastic volume elements, *Materials* 12 (3) (2019).
- [13] D. E. Sommer, S. G. Kravchenko, B. R. Denos, A. J. Favaloro, R. B. Pipes, Integrative analysis for prediction of process-induced, orientation-dependent tensile properties in a stochastic prepreg platelet molded composite, *Composites Part A: Applied Science and Manufacturing* 130 (2020) 105759.
- [14] N. Meyer, L. Schöttl, L. Bretz, A. Hrymak, L. Kärger, Direct bundle simulation approach for the compression molding process of sheet molding compound, *Composites Part A: Applied Science and Manufacturing* 132 (2020) 105809.
- [15] N. Meyer, A. Hrymak, L. Kärger, Modeling Short-Range Interactions in Concentrated Newtonian Fiber Bundle Suspensions, *International Polymer Processing* 36 (3) (2021) 255–263.
- [16] N. Meyer, Mesoscale simulation of the mold filling process of sheet molding compound, Ph.D. thesis, *Karlsruher Institut für Technologie (KIT)* (2021).
- [17] N. Meyer, S. Ilinzeer, A. Hrymak, F. Henning, L. Kärger, Non-isothermal direct bundle simulation of SMC compression molding with a non-Newtonian compressible matrix, *Journal of Non-Newtonian Fluid Mechanics* (submitted) (2022).
- [18] J. Görthofer, M. Schneider, F. Ospald, A. Hrymak, T. Böhlke, Computational homogenization of sheet molding compound composites based on high fidelity representative volume elements, *Computational Materials Science* 174 (2020) 109456.
- [19] J. Görthofer, M. Schneider, A. Hrymak, T. Böhlke, A convex anisotropic damage model based on the compliance tensor, *International Journal of Damage Mechanics* 31 (1) (2022) 43–86.
- [20] J. Görthofer, M. Schneider, A. Hrymak, T. Böhlke, A computational multiscale model for anisotropic failure of sheet molding compound composites, *Composite Structures* 288 (2022) 115322.
- [21] S. Gajek, M. Schneider, T. Böhlke, On the micromechanics of deep material networks, *Journal of the Mechanics and Physics of Solids* 142 (2020) 103984.
- [22] S. Gajek, M. Schneider, T. Böhlke, An FE-DMN method for the multiscale analysis of short fiber reinforced plastic components, *Computer Methods in Applied Mechanics and Engineering* 384 (2021) 113952.
- [23] S. Gajek, M. Schneider, T. Böhlke, Efficient two-scale simulations of microstructured materials using deep material networks, *PAMM* 21 (1) (2021) e202100069.

- [24] S. Gajek, M. Schneider, T. Böhlke, An FE-DMN method for the multiscale analysis of thermomechanical composites, *Computational Mechanics* 69 (5) (2022) 1087–1113.
- [25] A. Trauth, Characterisation and Modelling of Continuous-Discontinuous Sheet Moulding Compound Composites for Structural Applications, Doctoral thesis, Karlsruhe Institute of Technology (KIT), Karlsruhe, Germany (2020).
- [26] P. T. Odenberger, H. M. Andersson, T. S. Lundström, Experimental flow-front visualisation in compression moulding of SMC, *Composites Part A: Applied Science and Manufacturing* 35 (10) (2004) 1125–1134.
- [27] M. R. Barone, D. A. Caulk, Kinematics of flow in sheet molding compounds, *Polymer Composites* 6 (2) (1985) 105–109.
- [28] M. R. Barone, D. A. Caulk, A Model for the Flow of a Chopped Fiber Reinforced Polymer Compound in Compression Molding, *Journal of Applied Mechanics* 53 (1986) 361–371.
- [29] L. M. Abrams, J. M. Castro, Predicting molding forces during sheet molding compound (SMC) compression molding. I: Model development, *Polymer Composites* 24 (3) (2003) 291–303.
- [30] P. J. J. Dumont, L. Orgéas, D. Favier, P. Pizette, C. Venet, Compression moulding of SMC: In situ experiments, modelling and simulation, *Composites Part A: Applied Science and Manufacturing* 38 (2) (2007) 353–368.
- [31] M. Hohberg, L. Kärger, D. Bücheler, F. Henning, Rheological In-Mold Measurements and Characterizations of Sheet-Molding-Compound (SMC) Formulations with Different Constitution Properties by Using a Compressible Shell Model, *International Polymer Processing* 32 (5) (2017) 659–668.
- [32] G. B. Jeffery, The motion of ellipsoidal particles immersed in a viscous fluid, *Proceedings of the Royal Society of London. Series A, Containing Papers of a Mathematical and Physical Character* 102 (715) (1922) 161–179.
- [33] P. Dumont, S. Le Corre, L. Orgéas, D. Favier, C. Gaborit, P. Lory, Finite element implementation of a two-phase model for compression molding of composites, *Revue Europeenne des Elements* 14 (6-7) (2005) 885–902.
- [34] M. Perez, S. Guevelou, E. Abisset-Chavanne, F. Chinesta, R. Keunings, From dilute to entangled fibre suspensions involved in the flow of reinforced polymers: A unified framework, *Journal of Non-Newtonian Fluid Mechanics* 250 (2017) 8–17.

- [35] M. Perez, D. Prono, C. Ghnatios, E. Abisset-Chavanne, J. L. Duval, F. Chinesta, Advanced modeling and simulation of sheet moulding compound (SMC) processes, *International Journal of Material Forming* (2019) 1–11.
- [36] T.-H. Le, P. J. J. Dumont, L. Orgéas, D. Favier, L. Salvo, E. Boller, X-ray phase contrast microtomography for the analysis of the fibrous microstructure of SMC composites, *Composites Part A: Applied Science and Manufacturing* 39 (1) (2008) 91–103.
- [37] O. Guiraud, L. Orgéas, P. J. J. Dumont, S. Rolland du Roscoat, Microstructure and deformation micromechanisms of concentrated fiber bundle suspensions: An analysis combining x-ray microtomography and pull-out tests, *Journal of Rheology* 56 (3) (2012) 593–623.
- [38] A. Motaghi, A. N. Hrymak, Microstructure characterization in direct sheet molding compound, *Polymer Composites* 40 (S1) (2019) E69–E77.
- [39] D. J. Benson, Computational methods in Lagrangian and Eulerian hydrocodes, *Computer Methods in Applied Mechanics and Engineering* 99 (2-3) (1992) 235–394.
- [40] D. J. Benson, S. Okazawa, Contact in a multi-material Eulerian finite element formulation, *Computer Methods in Applied Mechanics and Engineering* 193 (39-41) (2004) 4277–4298.
- [41] M. Hohberg, L. Kärger, F. Henning, A. N. Hrymak, Rheological measurements and rheological shell model considering the compressible behavior of long fiber reinforced sheet molding compound (SMC), *Composites Part A: Applied Science and Manufacturing* 95 (2017) 110–117.
- [42] C. Krauß, L. Kärger, Tensor interpolation in virtual manufacturing chains for fiber reinforced composites, *International Journal of Mechanical Sciences* 226 (2022) 107378.
- [43] D. Krajcinovic, Continuum damage mechanics, *Applied Mathematics Reviews* 37 (1984) 1–6.
- [44] J. Lemaitre, Local approach of fracture, *Engineering Fracture Mechanics* 25 (5) (1986) 523 – 537.
- [45] D. Krajcinovic, Damage Mechanics, *Mechanics of Materials* 8 (1989) 3647–3679.
- [46] N. R. Hansen, H. L. Schreyer, A thermodynamically consistent framework for theories of elastoplasticity coupled with damage, *International Journal of Solids and Structures* 31 (3) (1994) 359–389.
- [47] J. Fitoussi, N. Bourgeois, G. Guo, D. Baptiste, Prediction of the anisotropic damaged behavior of composite materials: introduction of multilocal failure criteria in a micro-macro relationship, *Computational Materials Science* 5 (1996) 87–100.

- [48] G. Guo, J. Fitoussi, D. Baptiste, Modelling of damage behavior of a short-fiber reinforced composite structure by the finite element analysis using a micro-macro law, *International Journal of Damage Mechanics* 6 (1997) 278–299.
- [49] X. Z. Liu, H. H. Zhu, J. W. Ju, Q. Chen, Z. W. Jiang, Z. G. Yan, Investigation of the unbiased probabilistic behavior of the fiber-reinforced concrete's elastic moduli using stochastic micromechanical approach, *International Journal of Damage Mechanics* 29 (7) (2020) 1059–1075.
- [50] M. Franko, M. Sedláček, B. Podgornik, M. Nagode, Validation of linear damage rules using random loading, *International Journal of Damage Mechanics* 26 (3) (2017) 463–469.
- [51] J. W. Ju, Y. Wu, Stochastic micromechanical damage modeling of progressive fiber breakage for longitudinal fiber-reinforced composites, *International Journal of Damage Mechanics* 25 (2) (2016) 203–227.
- [52] Y. Wu, J. W. Ju, Elastoplastic damage micromechanics for continuous fiber-reinforced ductile matrix composites with progressive fiber breakage, *International Journal of Damage Mechanics* 26 (1) (2017) 3–27.
- [53] M. Schemmann, J. Görthofer, T. Seelig, A. Hrymak, T. Böhlke, Anisotropic meanfield modeling of debonding and matrix damage in SMC composites, *Composites Science and Technology* 161 (2018) 143–158.
- [54] X. Li, X. Qu, C. Qi, Z. Shao, An analytical model of multi-stress drops triggered by localized microcrack damage in brittle rocks during progressive failure, *International Journal of Damage Mechanics* 29 (9) (2020) 1345–1360.
- [55] M. Moradi, A. R. Bagherieh, M. R. Esfahani, Constitutive modeling of steel fiber-reinforced concrete, *International Journal of Damage Mechanics* 29 (3) (2020) 388–412.
- [56] A. Sharma, S. Daggumati, Computational micromechanical modeling of transverse tensile damage behavior in unidirectional glass fiber-reinforced plastic composite plies: Ductile versus brittle fracture mechanics approach, *International Journal of Damage Mechanics* 29 (6) (2020) 943–964.
- [57] A. S. Rahimi, M. R. Ayatollahi, A. R. Torabi, Elastic-plastic damage prediction in notched epoxy resin specimens under mixed mode I/II loading using two virtual linear elastic failure criteria, *International Journal of Damage Mechanics* 29 (7) (2020) 1100–1116.
- [58] S. Murakami, N. Ohno, A Continuum Theory of Creep and Creep Damage, in: A. Ponter, D. Hayhurst (Eds.), *Creep in Structures*, Springer, Berlin, Heidelberg, 1981, pp. 422–444.

- [59] Q. Wei, B. Gu, B. Sun, Ballistic penetration damages and energy absorptions of stacked cross-ply composite fabrics and laminated panels, *International Journal of Damage Mechanics* 29 (9) (2020) 1465–1484.
- [60] T. Okabe, S. Onodera, Y. Kumagai, Y. Nagumo, Continuum damage mechanics modeling of composite laminates including transverse cracks, *International Journal of Damage Mechanics* 27 (6) (2018) 877–895.
- [61] S. Onodera, T. Okabe, Analytical model for determining effective stiffness and mechanical behavior of polymer matrix composite laminates using continuum damage mechanics, *International Journal of Damage Mechanics* 29 (10) (2020) 1512–1542.
- [62] M. Alabdullah, N. M. Ghoniem, A thermodynamics-based damage model for the non-linear mechanical behavior of SiC/SiC ceramic matrix composites in irradiation and thermal environments, *International Journal of Damage Mechanics* 29 (10) (2020) 1569–1599.
- [63] M. Ortiz, E. P. Popov, A physical model for inelasticity of concrete, *Proceedings of the Royal Society A* 383 (1982) 101–125.
- [64] M. Ortiz, A constitutive theory for the inelastic behavior of concrete, *Mechanics of Materials* 4 (1) (1985) 67–93.
- [65] S. Yazdani, H. L. Schreyer, Combined plasticity and damage mechanics model for plain concrete, *Journal of Engineering Mechanics* 116 (1990) 1435–1450.
- [66] J. Simo, J. Ju, Strain- and stress-based continuum damage models - I. Formulation, *International Journal of Solids and Structures* 23 (7) (1987) 821–840.
- [67] J. W. Ju, On energy-based coupled elastoplastic damage theories: Constitutive modeling and computational aspects, *International Journal of Solids and Structures* 25 (7) (1989) 803–833.
- [68] R. de Borst, Softening, damage and higher-order continua, *Proceedings of the 2nd Conference on Fracture Mechanics of Concrete Structures* 1 (1996) 1631–1640.
- [69] T. Belytschko, Bažant, Zdeněk P., Y.-W. Hyun, T.-P. Chang, Strain-Softening Materials and Finite-Element Solutions, *Computers and Structures* 23 (2) (1986) 163–180.
- [70] Z. P. Bažant, Why Continuum Damage is Nonlocal: Micromechanics Arguments, *Journal of Engineering Mechanics* 117 (5) (1991) 1070–1087.
- [71] M. Brünig, S. Ricci, Nonlocal continuum theory of anisotropically damaged metals, *International Journal of Plasticity* 21 (7) (2005) 1346–1382.

- [72] R. K. Abu Al-Rub, G. Z. Voyiadjis, Gradient-enhanced coupled plasticity-anisotropic damage model for concrete fracture: Computational aspects and applications, *International Journal of Damage Mechanics* 18 (2) (2009) 115–154.
- [73] P. Junker, J. Riesselmann, D. Balzani, Efficient and robust numerical treatment of a gradient-enhanced damage model at large deformations, *International Journal for Numerical Methods in Engineering* 123 (3) (2022) 774–793.
- [74] G. Pijaudier-Cabot, Z. P. Bažant, Nonlocal Damage Theory, *Journal of Engineering Mechanics* 113 (10) (1987) 1512–1533.
- [75] E. C. Aifantis, On the Microstructural Origin of Certain Inelastic Models, *Journal of Engineering Materials and Technology* 106 (4) (1984) 326–330.
- [76] D. Balzani, M. Ortiz, Relaxed incremental variational formulation for damage at large strains with application to fiber-reinforced materials and materials with truss-like microstructures, *International Journal for Numerical Methods in Engineering* 92 (6) (2012) 551–570.
- [77] T. Schmidt, D. Balzani, Relaxed incremental variational approach for the modeling of damage-induced stress hysteresis in arterial walls, *Journal of the Mechanical Behavior of Biomedical Materials* 58 (2016) 149–162.
- [78] S. Schwarz, P. Junker, K. Hackl, Variational regularization of damage models based on the emulated RVE, *Continuum Mechanics and Thermodynamics* 33 (2021) 69–95.
- [79] S. Forest, C. Berdin, J. Besson, S. Bugat, E. Lorentz, *Local Approach to Fracture*, Les Presses de l’Ecole des Mines, Paris, 2004.
- [80] N. Halphen, Q. Nguyen, Sur les matériaux standards généralisés, *Journal de Mécanique* 14 (1975) 508–520.
- [81] J. Borwein, A. Lewis, *Convex Analysis and Nonlinear Optimization: Theory and Examples*, Springer, New York, 2006.
- [82] W. Karush, Minima of functions of several variables with inequalities as side constraints, Master’s thesis, Department of Mathematics, University of Chicago, Chicago (1939).
- [83] H. W. Kuhn, A. W. Tucker, Nonlinear programming, in: J. Neyman (Ed.), *Proceedings of the Second Berkeley Symposium on Mathematical Statistics and Probability*, University of California Press, Berkeley, 1951, pp. 481–492.

- [84] S. Wulfinghoff, M. Fassin, S. Reese, A damage growth criterion for anisotropic damage models motivated from micromechanics, *International Journal of Solids and Structures* 121 (2017) 21–32.
- [85] F. Meraghni, C. J. Blakeman, M. L. Benzeggagh, Effect of interfacial decohesion on stiffness reduction in a random discontinuous-fibre composite containing matrix microcracks, *Composites Science and Technology* 56 (5) (1996) 541–555.
- [86] A. Ben Cheikh Larbi, K. Sai, H. Sidhom, D. Baptiste, Constitutive Model of Micromechanical Damage to Predict Reduction in Stiffness of a Fatigued SMC Composite, *Journal of Materials Engineering and Performance* 15 (5) (2006) 575–580.
- [87] A. Trauth, P. Pinter, K. Weidenmann, Investigation of Quasi-Static and Dynamic Material Properties of a Structural Sheet Molding Compound Combined with Acoustic Emission Damage Analysis, *Journal of Composites Science* 1 (2) (2017) 18.
- [88] L. Schöttl, P. Kolb, W. V. Liebig, K. A. Weidenmann, K. Inal, P. Elsner, Crack characterization of discontinuous fiber-reinforced composites by using micro-computed tomography: Cyclic in-situ testing, crack segmentation and crack volume fraction, *Composites Communications* 21 (2020) 100384.
- [89] A. Puck, H. Schürmann, Failure analysis of FRP laminates by means of physically based phenomenological models, *Composite Science and Technology* 62 (2002) 1633–1662.
- [90] M. Knops, *Analysis of Failure in Fiber Polymer Laminates: The Theory of Alfred Puck*, Springer, Berlin, Heidelberg and New York, 2008.
- [91] A. Krawietz, Passivity, convexity and normality of elastic-plastic materials, *Ingenieur-Archiv* 51 (1981) 257–274.
- [92] A. Krawietz, Efficient Integration in the Plasticity of Crystals with Pencil Glide and Deck Glide, *Technische Mechanik* 21 (4) (2001) 243–250.
- [93] J. Renard and M. F. Marmonier, Etude de l’initiation de l’endommagement dans la matrice d’un matériau composite par une méthode d’homogenisation, *Aerospace Science and Technology* 9 (1987) 37 – 51.
- [94] R. J. M. Smit and W. A. M. Brekelmans and H. E. H. Meijer, Prediction of the mechanical behavior of nonlinear heterogeneous systems by multi-level finite element modeling, *Computer Methods in Applied Mechanics and Engineering* 155 (1) (1998) 181 – 192.
- [95] F. Feyel, Multiscale FE2 elastoviscoplastic analysis of composite structures, *Computational Materials Science* 16 (1) (1999) 344 – 354.

- [96] H. Moulinec, P. Suquet, A fast numerical method for computing the linear and nonlinear mechanical properties of composites, *Comptes Rendus de l'Académie des Sciences. Série II* 318 (11) (1994) 1417–1423.
- [97] H. Moulinec, P. Suquet, A numerical method for computing the overall response of nonlinear composites with complex microstructure, *Computer Methods in Applied Mechanics and Engineering* 157 (1998) 69–94.
- [98] M. Schneider, A review of nonlinear FFT-based computational homogenization methods, *Acta Mechanica* 232 (2021) 2051–2100.
- [99] J. Spahn and H. Andrä and M. Kabel and R. Müller, A multiscale approach for modeling progressive damage of composite materials using fast Fourier transforms, *Computer Methods in Applied Mechanics and Engineering* 268 (2014) 871–883.
- [100] J. Kochmann and S. Wulfinghoff and S. Reese and J. R. Mianroodi and B. Svendsen, Two-scale FE–FFT- and phase-field-based computational modeling of bulk microstructural evolution and macroscopic material behavior, *Computer Methods in Applied Mechanics and Engineering* 305 (2016) 89 – 110.
- [101] G. Dvorak, Y. Benveniste, On transformation strains and uniform fields in multiphase elastic media, *Proceedings of the Royal Society A* 437 (1992) 291–310.
- [102] G. Dvorak, Y. Bahei-El-Din, A. Wafa, Implementation of the transformation field analysis, *Computational Mechanics* 14 (14) (1994) 201–228.
- [103] G. Dvorak, Y. Bahei-El-Din, A. Wafa, The modeling of inelastic composite materials with the transformation field analysis, *Modelling and Simulation in Material Science and Engineering* 2 (2) (1994) 571–586.
- [104] Z. Liu, M. A. Bessa, W. K. Liu, Self-consistent clustering analysis: An efficient multi-scale scheme for inelastic heterogeneous materials, *Computer Methods in Applied Mechanics and Engineering* 306 (2016) 319–341.
- [105] Z. Liu, O. L. Kafka, C. Yu, W. K. Liu, Data-driven self-consistent clustering analysis of heterogeneous materials with crystal plasticity, in: *Advances in Computational Plasticity*, Springer, 2018, pp. 221–242.
- [106] Z. Liu, M. Fleming, W. K. Liu, Microstructural material database for self-consistent clustering analysis of elastoplastic strain softening materials, *Computer Methods in Applied Mechanics and Engineering* 330 (2018) 547–577.
- [107] J. C. Michel, P. Suquet, Nonuniform transformation field analysis, *International Journal of Solids and Structures* 40 (2003) 6937–6955.

- [108] J.-L. Chaboche, P. Kanouté, A. Roos, On the capabilities of mean-field approaches for the description of plasticity in metal matrix composites, *International Journal of Plasticity* 21 (2005) 1409–1434.
- [109] M. Schneider, On the mathematical foundations of the self-consistent clustering analysis for non-linear materials at small strains, *Computer Methods in Applied Mechanics and Engineering* 354 (2019) 783–801.
- [110] F. Fritzen, T. Böhlke, Reduced basis homogenization of viscoelastic composites, *Composites Science and Technology* 76 (2013) 84–91.
- [111] R. Largeton, J.-C. Michel, P. Suquet, Extension of the nonuniform transformation field analysis to linear viscoelastic composites in the presence of aging and swelling, *Mechanics of Materials* 73 (2014) 76–100.
- [112] M. N. Jadid, Prediction of Stress-strain Relationships for Reinforced Concrete Sections by Implementing Neural Network Techniques, *Journal of King Saud University - Engineering Sciences* 9 (2) (1997) 169–188.
- [113] D. Penumadu and R. Zhao, Triaxial compression behavior of sand and gravel using artificial neural networks (ANN), *Computers and Geotechnics* 24 (3) (1999) 207 – 230.
- [114] G. Srinivasu, R. N. Rao, T. K. Nandy, A. Bhattacharjee, Artificial neural network approach for prediction of titanium alloy stress-strain curve, *Procedia Engineering* 38 (2012).
- [115] M. Mozaffar and R. Bostanabad and W. Chen and K. Ehmann and J. Cao and M. A. Bessa, Deep learning predicts path-dependent plasticity, *Proceedings of the National Academy of Sciences* 116 (52) (2019) 26414–26420.
- [116] A. Koeppel and F. Bamer and B. Markert, An efficient Monte Carlo strategy for elasto-plastic structures based on recurrent neural networks, *Acta Mechanica* 230 (2019) 3279–3293.
- [117] M. B. Gorji and M. Mozaffar and J. N. Heidenreich and J. Cao and D. Mohr, On the potential of recurrent neural networks for modeling path dependent plasticity, *Journal of the Mechanics and Physics of Solids* 143 (2020) 103972.
- [118] Z. Liu, C. T. Wu, M. Koishi, A deep material network for multiscale topology learning and accelerated nonlinear modeling of heterogeneous materials, *Computer Methods in Applied Mechanics and Engineering* 345 (2019) 1138–1168.
- [119] Z. Liu, C. T. Wu, Exploring the 3D architectures of deep material network in data-driven multiscale mechanics, *Journal of the Mechanics and Physics of Solids* 127 (2019) 20–46.

- [120] D. Bücheler, Locally continuous-fiber reinforced sheet molding compound, Doctoral thesis, Wissenschaftliche Schriftenreihe des Fraunhofer ICT Nr. 79, Karlsruhe Institute of Technology (KIT), Fraunhofer Verlag, Stuttgart (2018).
- [121] Z. Liu, C. T. Wu, M. Koishi, Transfer learning of deep material network for seamless structure–property predictions, *Computational Mechanics* 64 (2) (2019) 451–465.
- [122] Z. Liu, H. Wei, T. Huang, C. T. Wu, Intelligent multiscale simulation based on process-guided composite database, arXiv preprint 2003.09491 (2020).
- [123] T. Mori, K. Tanaka, Average stress in matrix and average elastic energy of materials with misfitting inclusions, *Acta Metallurgica* 21 (5) (1973) 571–574.
- [124] L. Schöttl, D. Dörr, P. Pinter, K. A. Weidenmann, P. Elsner, L. Kärger, A novel approach for segmenting and mapping of local fiber orientation of continuous fiber-reinforced composite laminates based on volumetric images, *NDT & E International* 110 (2020) 102194.
- [125] L. Schöttl, K. A. Weidenmann, T. Sabiston, K. Inal, P. Elsner, Fiber bundle tracking method to analyze sheet molding compound microstructure based on computed tomography images, *NDT & E International* 117 (2021) 102370.
- [126] W. M. Bolstad, J. M. Curran, *Introduction to Bayesian Statistics*, John Wiley & Sons, Inc., Hoboken, New Jersey, 2016.
- [127] C. K. I. Williams, C. E. Rasmussen, *Gaussian Processes for Machine Learning*, Vol. 2, The MIT press, 2006.
- [128] A. Protim Dey, F. Welschinger, M. Schneider, S. Gajek, T. Böhlke, Training deep material networks to reproduce creep loading of short fiber-reinforced thermoplastics with an inelastically-informed strategy, *Archive of Applied Mechanics* (accepted) (2022).
- [129] M. Kabel, S. Fliegner, M. Schneider, Mixed boundary conditions for FFT-based homogenization at finite strains, *Computational Mechanics* 57 (2) (2016) 193–210.
- [130] M. Schneider, M. Josien, F. Otto, Representative volume elements for matrix-inclusion composites – a computational study on the effects of an improper treatment of particles intersecting the boundary and the benefits of periodizing the ensemble, *Journal of the Mechanics and Physics of Solids* 158 (2022) 104652.
- [131] D. E. Tyler, Statistical analysis for the angular central Gaussian distribution on the sphere, *Biometrika* 74 (3) (1987) 579–589.
- [132] J. Feder, Random sequential adsorption, *Journal of Theoretical Biology* 87 (2) (1980) 237–254.

- [133] I. M. Sobol', On the distribution of points in a cube and the approximate evaluation of integrals, USSR Computational Mathematics and Mathematical Physics 7 (4) (1967) 86–112.